Biogeosciences Discuss., 9, 16161–16211, 2012
www.biogeosciences-discuss.net/9/16161/2012/
doi:10.5194/bgd-9-16161-2012

Biogeosciences Discussions

Spectrally resolved efficiencies of carbon monoxide (CO) photoproduction in the Western Canadian Arctic: particles versus solutes

G. Song[1], H. Xie[1], S. Bélanger[2], and M. Babin[3]

[1]Institut des sciences de la mer de Rimouski, Université du Québec à Rimouski, Rimouski (Québec), G5L 3A1 Canada
[2]Département de biologie, chimie et géographie and BORÉAS, Université du Québec à Rimouski, Rimouski (Québec), G5L 3A1 Canada
[3]Takuvik Joint International Laboratory (CNRS & ULaval), Département de Biologie, Québec-Océan and Arcticnet, Université Laval, Québec (Québec), G1V 0A6 Canada

Received: 17 September 2012 – Accepted: 31 October 2012 – Published: 15 November 2012

Correspondence to: H. Xie (huixiang_xie@uqar.qc.ca)

Published by Copernicus Publications on behalf of the European Geosciences Union.

Abstract

Spectrally resolved efficiency (i.e. apparent quantum yield, AQY) of carbon monoxide (CO) photoproduction is a useful indicator of substrate photoreactivity and a crucial parameter for modeling CO photoproduction rates in the water column. Recent evidence has suggested that CO photoproduction from particles in marine waters is significant compared to the well-known CO production from chromophoric dissolved organic matter (CDOM) photodegradation. Although CDOM-based CO AQY spectra have been extensively determined, little is known of this information on the particulate phase. Using water samples collected from the Mackenzie estuary, shelf, and Canada Basin in the Southeastern Beaufort Sea, the present study for the first time quantified the AQY spectra of particle-based CO photoproduction and compared them with the concomitantly determined CDOM-based CO AQY spectra. CO AQYs of both particles and CDOM decreased with wavelength but the spectral shape of the particulate AQY was flatter in the visible regime. This feature resulted in a disproportionally higher visible light-driven CO production by particles, thereby increasing the ratio of particle- to CDOM-based CO photoproduction with depth in the euphotic zone. In terms of depth-integrated production in the euphotic zone, CO formation from CDOM was dominated by the ultraviolet (UV, 290–400 nm) radiation whereas UV and visible light played roughly equal roles in CO production from particles. Spatially, CO AQY of bulk particulate matter (i.e. the sum of organics and inorganics) augmented from the estuary to shelf to basin while CO AQY of CDOM trended inversely. Water from the deep chlorophyll maximum layer revealed higher CO AQYs than did surface water for both particles and CDOM. CO AQY of bulk particulate matter exceeded that of CDOM on the shelf and in the basin but the sequence reversed in the estuary. Mineral absorption-corrected CO AQY of particulate organic matter (POM) was, however, greater than its CDOM counterpart in all three sub-regions and displayed magnitudes in the estuary that were no inferior to those in shelf and offshore waters. In terms of CO photoproduction, POM was thus more photoreactive than CDOM, irrespective of the

BGD
9, 16161–16211, 2012

organic matter's origins (i.e. terrigenous or marine). Riverine CDOM exhibited higher photoreactivity than marine CDOM and land-derived POM appeared similarly or more photoreactive than marine POM. AQY-based modeling indicates that CO photoproduction in the study area is underestimated by 13–48 % if the particulate term is ignored.

1 Introduction

The absorption of solar ultra-violet (UV) and visible radiation by chromophoric dissolved organic matter (CDOM) initiates a myriad of chemical reactions that significantly impact the ocean's biogeochemical cycles of carbon, nitrogen, sulfur, trace metals, and trace gases (Mopper and Kieber, 2002). Examples of CDOM photoprocesses that have been or are being extensively studied include (1) the formation of environmentally and biologically reactive oxygen species, such as HO·, $O_2^{\cdot-}$, and H_2O_2 (Zafiriou et al., 1984; Blough and Zepp, 1995); (2) the remineralization of dissolved organic carbon (DOC) to carbon dioxide (CO_2) and carbon monoxide (CO) (Miller and Zepp, 1995); (3) the conversion of refractory DOC to labile substrates (Kieber et al., 1989; Miller et al., 2002) or vice versa (Kieber et al., 1997; Benner and Biddanda, 1998); (4) the generation of bioavailable inorganic nitrogen, mainly ammonium, from bioinert dissolved organic nitrogen (DON) (Bushaw et al., 1996; Vähätalo and Zepp, 2005); (5) the alteration of the redox state of certain metals, such as Fe and Cu, and hence their toxicity or bioavailability (Miller et al., 1995; Voelker and Sedlak, 1995; Voelker et al., 2000); (6) the production or decomposition of some biologically and atmospherically active sulfur-containing gases, such as carbonyl sulfide and dimethyl sulfide (Brimblecombe, 2003); (7) the degradation of several important biomarkers, e.g. lignin, amino acids (Opsahl and Benner, 1998; Benner and Kaiser, 2010); (8) the destruction of CDOM's UV-absorbing chromophores and its implication for marine optics and ecology (Zepp, 2003). In contrast to the colossal efforts and progress made in CDOM photochemistry, much less attention has been paid to particulate organic matter (POM) with the exception of photodegradation of chlorophylls and unsaturated lipids of phytoplankton

BGD
9, 16161–16211, 2012

(e.g. SooHoo and Kiefer, 1982; Nelson, 1993; Rontani, 2001; Rontani, et al., 2011). The similarity in the absorption spectrum between POM and CDOM (Kirk, 1980), however, suggests that POM may undergo photochemical processes analogous to those of CDOM. Besides, a rich POM photochemistry could be favored by the fact that particles adsorb organics at their surfaces, often abound with photoreactive metals (e.g. Fe, Cu, Mn), and carry localized microenvironments of extremely high concentrations of reactants (Zafiriou, 2002). Early studies have demonstrated that irradiation of detritus of certain vascular plants produces CO (Tarr et al., 1995) and CO_2 (Anesio et al., 1999a) and releases DOC (Anesio et al., 1999b). More recently, a few groups have reported significant losses of particulate organic carbon (POC) and productions of DOC, CO_2, DON, and CDOM from controlled irradiation of resuspensions of river and coastal sediments (Kieber et al., 2006; Riggsbee et al., 2008; Pisani et al., 2011; Shank et al., 2011). Similar results have been found for phytoplankton detritus, with an added finding of ammonium production (Mayer et al., 2009; Estapa and Mayer, 2010).

Although laboratory irradiation experiments suggest potentially significant biogeochemical cycling rates resulting from POM photodegradation, extrapolating these results to real environments often entails potentially large uncertainties due partly to limited sample coverage and the inability of controlled incubations to adequately simulate the more complex optical, chemical, and hydrological conditions occurring in natural waters (Mayer et al., 2009; Estapa and Mayer, 2010). Moreover, the lack of information on the spectral efficiency (also termed apparent quantum yield, AQY) of POM photoprocesses makes it difficult to estimate their fluxes on different spatiotemporal scales using coupled optical-photochemical modeling, an approach that has been widely applied to CDOM photochemistry (e.g. Zafiriou et al., 2003; Xie et al., 2009; Fichot and Miller, 2010). It remains, therefore, unclear as to whether POM photodegradation in natural marine ecosystems can effectively affect organic matter and elemental cycles and how important this process is in comparison with CDOM photochemistry.

Here we report the measurement of AQY spectra of CO photoproduction from suspended particulate matter (SPM) in the Western Canadian Arctic and a direct

BGD
9, 16161–16211, 2012

comparison between the particle- and CDOM-based CO efficiencies. To the best of our knowledge, these are the first published spectral efficiency data for a POM photoproduct. We modeled CO photoproduction using the AQY spectra obtained and discussed the implication of POM photooxidation for the CO budget. CO was targeted for a number of reasons. First, a preliminary study evaluating CO photoproduction from particles suggested a significant POM-based term (up to 40 % of the CDOM-based component) in both coastal and oligotrophic marine waters (Xie and Zafiriou, 2009). Second, thanks to its low background concentrations and high analytical sensitivity, CO can be relatively easily and precisely (±2 %) quantified (Xie et al., 2002). Thus, even small signal changes due to POM photodegradation should be detectable. Third, the role of CO as a proxy species for other major but more-difficult-to-measure CDOM photoproducts (e.g. CO_2, biolabile carbon) (Miller and Zepp, 1995; Miller et al., 2002; White et al., 2010) could also hold for POM photochemistry. Finally, an assessment of the POM-based CO source helps better understand the physical and biogeochemical functions of this species, since CO is a useful tracer for modeling upper-ocean mixing dynamics (Kettle, 2005), an atmospherically active trace gas emitting from the ocean (Conrad et al., 1982; Stubbins et al., 2006a), and an energy source for bacteria oxidizing it (King and Weber, 2007; Moran and Miller, 2007).

2 Methods

2.1 Study area

The study area encompassed the Mackenzie River estuary (MRE), Mackenzie Shelf (MS), and Canada Basin (CB) in the Southeastern (SE) Beaufort Sea (Fig. 1). The area's most prominent hydrographic feature is the Mackenzie River, the only North American analogue to the immense Arctic rivers on the Siberian continent. The Mackenzie River possesses a watershed area of 1680 km^2 and delivers to the Arctic Ocean the largest POC (1.8–2.1 × 10^{12} g C yr^{-1}), sixth largest DOC (1.3 g C yr^{-1}),

BGD
9, 16161–16211, 2012

and fourth largest freshwater (249–333 $km^3 yr^{-1}$) fluxes among all major Arctic rivers (Dittmar and Kattner, 2003). The river flows into the Beaufort Sea through two major passages: the western and eastern channels. The river flow, subject to the Coriolis effect, bends to the right toward the Amundsen Gulf under calm conditions but can extend across the shelf into the interior ocean under strong easterly winds (Macdonald et al., 1999). CDOM in surface water is of primarily terrigenous origin on the shelf but has a strong autochthonous signature in the CB (Stedmon et al., 2011). Terrigenous particles dominate within the water column of the river plume, while particles of marine origin prevail outside the plume (Goñi et al., 2005; Forest et al., 2007; Magen et al., 2010). Water column primary production in the SE Beaufort Sea is limited by light availability prior to ice break in early spring but by nitrogen depletion subsequent to the spring phytoplankton bloom in water masses away from direct riverine and upwelling influences (Tremblay et al., 2008). The exhaustion of surface-water nitrogen typically leads to the formation of deep chlorophyll maxima (DCM) near the nutricline having Pacific summer water characteristics (Tremblay et al., 2008; Matsuoka et al., 2012).

The Western Canadian Arctic is one of the most sensitive regions on Earth to climate warming (Flato et al., 2000). Rising temperatures in this region over the last several decades have supposedly shortened sea ice-cover timespan and reduced sea ice extent (Stroeve et al., 2008), allowing more solar radiation to penetrate into the water column. Interests have since intensified concerning the fate and transformation of the terrigenous organic matter exported to the Arctic Ocean (Opsahl et al., 1999; Hansell et al., 2004; Benner et al., 2005). Photooxidation, a well-known CDOM sink in mid- and low-latitude oceans, has recently been proposed as a potentially significant cycling term of terrigenous CDOM in the Western Canadian Arctic seas (e.g. Bélanger et al., 2006; Xie et al., 2009; Osburn et al., 2009), since declining ice cover, combined with increasing solar UV radiation over the high north (Fioletov et al., 2004; see also website: http://onlinelibrary.wiley.com/doi/10.1002/wea.700/pdf), enhances the photooxidation potential in the water column.

BGD
9, 16161–16211, 2012

2.2 Sampling

Sampling was conducted during the Mackenzie Light and Carbon (Malina) Program in August 2009 aboard the icebreaker *CCGS Amundsen*, covering the MS (< 200 m deep) and CB (> 200 m deep) (Fig. 1). A Zodiac boat released from the *CCGS Amundsen* visited two salinity gradient transects (SGTs) characterized by shallow waters, each in the east (SGT-E) and west (SGT-W) channel of the MRE. SGT samples were collected using a clean high-density polyethylene bucket, transferred into 20-l acid-washed, collapsible polyethylene carboys, and then brought back to the *CCGS Amundsen*. Shelf and open ocean samples were taken at the surface (~ 3 m deep) and DCM (mostly 60–75 m deep) using 12-l Niskin bottles mounted onto a standard conductivity-temperature-depth (CTD) rosette. Detailed sampling information is compiled in Table 1. Niskin and bucket samples were gravity-pushed through Whatman Polycap 75 AS filtration capsules sequentially containing 0.2 µm glass microfiber and nylon membrane filters. The filtrates were collected into half-gallon clear glass bottles (Qorpak) for irradiation experiments (see below) and 60-ml clear glass bottles (Qorpak) for CDOM absorbance measurements. The capsules were thoroughly flushed with Nanopure water and then sample water prior to filtration. Unfiltered samples were directly transferred into half-gallon glass bottles for irradiation experiments and 2-l plastic bottles (Nalgene) for chlorophyll *a* (Chl *a*) and particle absorbance determinations. All bottles were protected against light during sample transfer by wrapping them with aluminum foil or black plastic bags. They were all sequentially acid-cleaned with 10 % HCl, profusely washed with Nanopure water, and rinsed with sample water before use. Irradiation experiments and particle optical density (i.e. absorbance) and Chl *a* concentration ([Chl *a*]) measurements were performed aboard the ship immediately after sample collection. CDOM samples, stored under refrigeration and darkness, were transported to Rimouski at the end of the cruise and analyzed immediately thereafter.

BGD
9, 16161–16211, 2012

2.3 Irradiation

Unfiltered water samples were poisoned with KCN (4.3 µmol l^{-1}) to eliminate microbial CO uptake and filtered samples were amended with the same amount of KCN for uniformity of sample treatment. Samples were purged with CO-free air to minimize background CO concentrations, transferred into pre-combusted, quartz-windowed cylindrical cells having an inner diameter of 3.4 cm and a length of 11.4 cm. The quartz cells were closed without headspace and placed vertically in a temperature-controlled (4 °C) incubator, and irradiated using a SUNSET XLS+ solar simulator equipped with a 1.5 kW xenon lamp. Radiation reaching the sample was essentially collimated and perpendicular to the irradiation surface (see Supporting Information in the study by Zhang et al. 2006). Parallel dark controls served to evaluate any thermal effects on CO production. A series of successive Schott long-band cutoff filters, with model numbers of WG280, WG295, WG320, WG345, GG395, GG435, and GG495, were employed to evaluate the wavelength dependence of CO photoproduction. Spectral photon fluxes impinging onto the window of each quartz cell were measured at 1 nm intervals using an OL-754 spectroradiometer fitted with a 2-inch OL IS- 270 integrating sphere. The variability of the lamp output across the UV and visible regimes was within 4 % throughout the entire cruise. Irradiation lasted up to 8.0 h (mostly < 3 h) for samples under cutoff filters WG280, WG295, and WG320 and up to 21.2 h for samples under the remaining longer cutoff filters. Estuarine and coastal samples were subject to shorter durations of exposure compared to open-ocean samples. More details on the irradiation setup and procedure are available elsewhere (Zhang et al., 2006).

2.4 Analyses

CO concentrations were measured using the headspace method reported by Xie et al. (2002). Briefly, post-irradiation samples were transferred to a 50-ml glass syringe, into which 5-ml CO-free air was introduced to obtain a 1 : 6 gas : water ratio. The syringe was vigorously shaken for 3 min and the equilibrated headspace gas was

BGD
9, 16161–16211, 2012

injected into a TA3000 Reduction Gas Analyzer (Trace Analytical) for CO quantification. The analyzer was standardized by frequent injections of a National Institute of Standards and Technology (NIST)-traceable gaseous CO standard of 1.23 parts per million by volume (Praxair). To be consistent with the samples' relative humidity (100 %), the dry CO standard was drawn into a wetted 10-ml glass before injection. The amount of CO photochemically produced was calculated as the difference in CO concentration between the irradiated sample and the parallel dark control.

For Chl *a* quantification, water samples (250–1000 ml) were filtered through precombusted 25-mm GF/F filters (Whatman) under low vacuum (< 50 kPa). The particles-retained filters were placed in 10 ml of 90 % acetone in scintillation vials for at least 18 h in the dark at 4 °C. The supernatants were analyzed for fluorescence before and after being acidified with 100 µl of 5 % HCl, using a Turner Designs fluorometer (model 10-AU) according to the method of Parsons et al. (1984). [Chl *a*]s were calculated using the equation of Holm-Hansen et al. (1965).

Water samples (5.0–2735 ml) for particle optical density measurement were subjected to the same filtration procedure as that for Chl *a* determination. Particulate matter collected on the filters was analyzed for optical density using a Perkin Elmer Lambda 19 dual beam spectrometer fitted with a 150-mm integrating sphere (Labsphere) accommodating a homemade filter holder (Röttgers and Gehnke, 2012). The spectral optical density of the filter, $OD_{f,\lambda}$, where λ is wavelength in nm, was recorded from 800 to 300 nm at 1-nm increments and a scanning speed of 120 nm min^{-1}. $OD_{f,\lambda}$ was converted to the spectral particulate absorption coefficient, $a_{p,\lambda}$ (m^{-1}), using Eq. (1),

$$a_{p,\lambda} = 2.303 \times (A/V) \times (OD_{f,\lambda} - OD_{blank,\lambda}) \times (1/\beta_\lambda) \quad (1)$$

where $OD_{blank,\lambda}$ is the optical density of a blank filter, A the clearance area of particles on the filter (m^2), V the volume of sample water filtered (m^3), and β_λ the path length amplification factor. Here we fitted β_λ nonlinearly to $OD_{f,\lambda}$ (Röttgers and Gehnke, 2012):

BGD
9, 16161–16211, 2012

$$\beta_\lambda = 2.9\mathrm{OD}_{\mathrm{f},\lambda}{}^2 - 4.76\mathrm{OD}_{\mathrm{f},\lambda} + 4.5 \quad (2)$$

Upon the completion of $a_{\mathrm{p},\lambda}$ determination, the filter was dipped in 10 ml methanol for ~ 18 h to bleach pigments and the absorption coefficient of non-algal particles, $a_{\mathrm{nap},\lambda}$ (m^{-1}), was determined in the same manner as that for $a_{\mathrm{p},\lambda}$. Data of $a_{\mathrm{p},\lambda}$ and $a_{\mathrm{nap},\lambda}$ between 250 and 299 nm were extrapolated from the exponential fits of $a_{\mathrm{p},\lambda}$ and $a_{\mathrm{nap},\lambda}$ to wavelength over the range from 300–420 nm. Subtracting $a_{\mathrm{nap},\lambda}$ from $a_{\mathrm{p},\lambda}$ gave the phytoplankton absorption coefficient, $a_{\mathrm{phy},\lambda}$ (m^{-1}). More details of particulate absorption measurement can be found in the study of Doxaran et al. (2012).

The spectral optical density of CDOM, $\mathrm{OD}_{\mathrm{cdom},\lambda}$, was scanned from 800 to 200 nm at 1-nm intervals using a Perkin–Elmer Lambda 35 dual beam spectrophotometer fitted with a 5-cm quartz flow cell and referenced to high-performance-liquid-chromatography (HPLC) grade pure water (Ricca Chemical). Samples were allowed to warm up to room temperature before analysis. The flow cell was rinsed with methanol, pure water, and sample water between individual scans. A baseline correction was applied by subtracting the optical density averaged over 683–687 nm from all $\mathrm{OD}_{\mathrm{cdom},\lambda}$ values (Babin et al., 2003). The spectral CDOM absorption coefficient, $a_{\mathrm{cdom},\lambda}$ (m^{-1}), was calculated as 2.303 times $\mathrm{OD}_{\mathrm{cdom},\lambda}$ divided by the light path length of the cell in meters (0.05 m). The lower detection limit of $a_{\mathrm{cdom},\lambda}$ determination, defined as three times the standard deviation of five replicate analyses of pure water, was $0.02 \pm 0.01\ \mathrm{m}^{-1}$ over 250–700 nm.

2.5 Retrieval of CO AQY

The spectral CO AQY, Φ_λ, is defined as the number of moles of CO produced per mole of photons absorbed by a given set of light-absorbing materials at wavelength λ. Here the light-absorbing materials refer to CDOM, particles, and CDOM plus particles, corresponding to Φ_λ for CDOM ($\Phi_{\mathrm{cdom},\lambda}$), particles ($\Phi_{\mathrm{p},\lambda}$), and total dissolved and particulate matter ($\Phi_{\mathrm{t},\lambda}$), respectively. The number of absorbed photons at wavelength λ,

BGD
9, 16161–16211, 2012

$Q_{a,\lambda}$ (mol photons s^{-1} nm^{-1}), was calculated using Eq. (3) (Hu et al., 2002):

$$Q_{a,\lambda} = Q_\lambda \times S \times \left(a_\lambda / a_{t,\lambda}\right) \times \left[1 - \exp\left(-a_{t,\lambda} \times L\right)\right] \quad (3)$$

Q_λ (mol photons m^{-2} s^{-1} nm^{-1}) denotes the photon flux just below the frontal quartz window; a_λ (m^{-1}) stands for $a_{cdom,\lambda}$ for filtered samples or $a_{cdom,\lambda}$ plus $a_{p,\lambda}$ for unfiltered samples; $a_{t,\lambda}$ (m^{-1}) is the total absorption coefficient, i.e. $a_{cdom,\lambda}$ plus the absorption coefficient of pure water,$a_{w,\lambda}$ (m^{-1}) (Buiteveld et al., 1994; Pope and Fry, 1997), for filtered samples or the sum of $a_{cdom,\lambda}$, $a_{p,\lambda}$, and $a_{w,\lambda}$ for unfiltered seawater; S (m^2) and L (m) are, respectively, the cross-section and path length of the irradiation cells. The contribution of particle backscattering to light attenuation in unfiltered samples was omitted since data available indicate that the backscattering coefficient (bb_m) on average accounted for only 2.1 % (range: 0.2–6.8 %, n = 10; 300–400 nm) of the diffuse attenuation coefficient ($k_d \approx a_t + bb_m$ under collimated light). This omission averagely underestimated Φ_t by 1.6 % (0.4 %–3.0 %) and Φ_p by 4.6 % (1.0 %–7.0 %) at Sta. 697, which had the highest $bb_m : k_d$ ratio (0.061–0.068). Additionally, the effect of scattering on the light path length under collimated radiation is minor since most of the scattering due to particles is at very small scattering angles in the forward direction (Mobley 1994).

$\Phi_{cdom,\lambda}$ and $\Phi_{t,\lambda}$ were obtained with an iterative curve-fit protocol developed by Johannessen and Miller (2001) and modified by Zhang et al. (2006). Briefly, this method assigned a quasi-exponential form with unknown parameters to express the change of Φ_λ ($\Phi_{cdom,\lambda}$ or $\Phi_{t,\lambda}$) as a function of wavelength (Zhang et al., 2006; Xie et al., 2009):

$$\Phi_\lambda = m_1 \times \exp\left[m_2/(\lambda + m_3)\right] \quad (4)$$

where m_1, m_2, and m_3 are fitting parameters. The amount of CO produced in an irradiation cell over the exposure time could then be predicted as the product of the assumed Φ_λ function and the number of absorbed photons integrated over 250–600 nm. The optimum values of the unknown parameters in Eq. (3) were computed by varying these parameters from initial estimates until the minimum difference between the measured

BGD
9, 16161–16211, 2012

and predicted production is achieved. CO production rates calculated from the retrieved Φ_λ were in good agreement with the measured rates, with R^2 ranging from 0.969 to 0.998 (mean: 0.991) for filtered samples and from 0.982 to 0.998 (mean: 0.992) for unfiltered samples.

$\Phi_{p,\lambda}$ can be derived from $\Phi_{cdom,\lambda}$ and $\Phi_{t,\lambda}$ per the following mathematical manipulations. The spectral CO photoproduction rate in an unfiltered sample, $P_{t,\lambda}$ (mol CO s^{-1} nm^{-1}), can be expressed as

$$P_{t,\lambda} = \Phi_{t,\lambda} \times Q_\lambda \times S \times \left[\left(a_{cdom,\lambda} + a_{p,\lambda}\right)/a_{t,\lambda}\right] \times [1 - \exp(-a_{t,\lambda} \times L)] \quad (5)$$

$P_{t,\lambda}$ is the sum of CO photoproduction from CDOM, $P_{cdom,\lambda}$ (mol CO s^{-1} nm^{-1}), and that from particles, $P_{p,\lambda}$ (mol CO s^{-1} nm^{-1}), i.e.

$$P_{t,\lambda} = P_{cdom,\lambda} + P_{p,\lambda} \quad (6)$$

$P_{cdom,\lambda}$ and $P_{p,\lambda}$ are given by

$$P_{cdom,\lambda} = \Phi_{cdom,\lambda} \times Q_\lambda \times S \times (a_{cdom,\lambda}/a_{t,\lambda}) \times [1 - \exp(-a_{t,\lambda} \times L)] \quad (7)$$

and

$$P_{p,\lambda} = \Phi_{p,\lambda} \times Q_\lambda \times S \times (a_{p,\lambda}/a_{t,\lambda}) \times [1 - \exp(-a_{t,\lambda} \times L)] \quad (8)$$

Substituting Eqs. (5), (7) and (8) into Eq. (6) and rearranging it give

$$\Phi_{p,\lambda} = \Phi_{t,\lambda} + (\Phi_{t,\lambda} - \Phi_{cdom,\lambda}) \times (a_{cdom,\lambda}/a_{p,\lambda}) \quad (9)$$

To facilitate comparison of various Φ_λ spectra, a solar irradiance spectrum-weighted mean apparent quantum yield, $\bar{\Phi}$, was computed for each CO AQY spectrum following the procedure of Xie et al. (2009):

$$\bar{\Phi} = \left(\int_{290}^{600} Q_{0,\lambda} \times \Phi_\lambda \times d\lambda\right) / \left(\int_{290}^{600} Q_{0,\lambda} \times d\lambda\right) \quad (10)$$

BGD
9, 16161–16211, 2012

$\bar{\Phi}$ denotes $\bar{\Phi}_{cdom}$ for CDOM, $\bar{\Phi}_p$ for particles, and $\bar{\Phi}_t$ for CDOM plus particles. $Q_{0,\lambda}$ (mol photons $m^{-2}\,h^{-1}\,nm^{-1}$) is the surface spectral solar photon fluxes at 70° N, 133° W at 14:00 LT on 1 July, simulated using the SMARTS model (Simple Model of the Atmospheric Radiative Transfer of Sunshine; Gueymard, 2001) under mid-summer Arctic atmospheric and cloudless conditions with an ozone column burden of 330 Dobson Units. This normalization reduced the AQY spectrum to a single value equivalent to the solar insolation-normalized production of CO in the entire water column in which all solar radiation over 290–600 nm was absorbed by a specific group of light-absorbing material, i.e. CDOM, particles, or the sum of the two (Bélanger et al., 2006).

3 Results and discussion

3.1 General physical, biological, and chemical settings

Salinity, temperature, [Chl *a*], and absorption coefficients of various constituents are shown in Table 2. Surface salinity along the SGT-W monotonically increased seaward from 0.15 at Sta. 697 to 23.61 at Sta. 691. The SGT-E covered a much narrower salinity range from 17.27 at Sta. 396 to 27.90 at Sta. 392. The lower mean surface salinity in the CB than that on the MS suggests a stronger influence of sea ice melting in the CB. Surface temperature along the SGTs displayed a trend inverse to salinity, decreasing seaward from 10.3 °C to 5.2 °C along the SGT-W and from 8.2 °C to 3.2 °C across the SGT-E; temperature further decreased from the MS to CB. Mean salinity and temperature of the DCM samples were 31.64 and −1.0 °C, respectively, typical of Pacific summer water origin (McLaughlin, 1996; Matsouka et al., 2012).

[Chl *a*] generally decreased from nearshore to offshore at both the surface and DCM. The highest value (7.6 $\mu g\,l^{-1}$) in the surface occurred at Sta. 170 located within the upwelling zone off Cape Bathurst (Williams and Carmack, 2008). Mean [Chl *a*]s at the DCM were 3.8 $\mu g\,l^{-1}$ on the MS and 0.42 $\mu g\,l^{-1}$ in the CB, being 2.4 and 5.2 times their surface values.

BGD
9, 16161–16211, 2012

The absorption coefficients of CDOM and particles at the surface, as exemplified by $a_{cdom,412}$ and $a_{p,412}$, diminished rapidly from the estuary to the MS and CB, indicating a strong influence of the riverine input of dissolved and particulate materials. The highest $a_{cdom,412}$ and $a_{p,412}$ both occurred at Sta. 697 ($a_{cdom,412}$: 2.04 m^{-1}; $a_{p,412}$: 8.40 m^{-1}) and the lowest in the ice melt-influenced water at Sta. 430 ($a_{cdom,412}$: 0.07 m^{-1}; $a_{p,412}$: 0.004 m^{-1}). Relatively high $a_{cdom,412}$ (0.20 m^{-1}) and $a_{p,412}$ (0.26 m^{-1}) values were observed in the upwelling zone (Sta. 170). At the DCM, $a_{cdom,412}$ was fairly constant throughout the MS and CB; $a_{p,412}$was more variable with the mean value for the MS being nine times that for the CB. The $a_{phy,412} : a_{p,412}$ ratio increased from nearshore to offshore, with the lowest occurring at Sta. 697 (0.06) and the highest at Sta. 430 (0.66). The mean $a_{phy,412} : a_{p,412}$ ratio at the DCM was ~2 times that at the surface in both the MS and CB.

3.2 CO AQY spectra

Fitted parameters for Eq. (3) are shown in Table 3 and typical $\Phi_{cdom,\lambda}$ and $\Phi_{p,\lambda}$ spectra are displayed in Fig. 2. $\Phi_{p,\lambda}$ at the innermost Sta. 697 on the SGT-W was lower than $\Phi_{cdom,\lambda}$, the difference being pronounced in the UV- A wavelengths. At Sta. 280 on the MS and Sta. 430 in the CB, surface water $\Phi_{p,\lambda}$ was higher than $\Phi_{cdom,\lambda}$ at $\lambda > 330$ nm, with the difference increasing with wavelength. Similarly, $\Phi_{p,\lambda}$ at the DCM both on the MS (Sta. 280) and in the CB (Sta. 345) exceeded $\Phi_{cdom,\lambda}$ by large extents over most spectral regimes (Fig. 2). Notably, the spectral patterns of $\Phi_{p,\lambda}$ for the more marine samples were characterized by conspicuous shoulders, particularly between 500 nm and 600 nm, contrasting with the rather smooth spectral shape of $\Phi_{p,\lambda}$ for the estuarine sample (Sta. 697). This spectral attribute might be linked to the relatively high pigment content in the saltier samples, especially at the DCM, as inferred from the $a_{phy} : a_p$ ratio (Table 2). Pigments such as chlorophylls and phaeopigments are often highly photoreactive (Nelson, 1993) but the spectral characteristics of CO photoproduction

BGD
9, 16161–16211, 2012

from these chromophores are unknown. A mechanistic study is needed to elucidate this point.

Figure 3 compares $\bar{\Phi}$ among the three sub-regions and between the surface and DCM. Mean surface water $\bar{\Phi}_{cdom}$ dropped by ~40 % from the estuary to the MS but only slightly decreased from the MS to the CB (6 %). On the contrary, mean surface water $\bar{\Phi}_p$ increased seaward, from 0.72×10^{-6} in the estuary to 0.98×10^{-6} on the MS to 1.46×10^{-6} in the CB. At the DCM, the mean $\bar{\Phi}_{cdom}$ on the MS (1.19×10^{-6}) was marginally higher than the mean $\bar{\Phi}_{cdom}$ in the CB (1.09×10^{-6}) while an opposing trend was observed for the mean $\bar{\Phi}_p$ (MS: 1.54×10^{-6} vs. CB: 2.04×10^{-6}). DCM's $\bar{\Phi}_{cdom}$ and $\bar{\Phi}_p$ were higher than their surface counterparts. The ratio of $\bar{\Phi}_p$ to $\bar{\Phi}_{cdom}$ was < 1 in the estuary (0.5) but > 1 in shelf and offshore waters at both the surface and DCM (range: 1.2–1.9). Surface and DCM samples exhibited comparable $\bar{\Phi}_p : \bar{\Phi}_{cdom}$ ratios with the highest values seen in the CB.

$\bar{\Phi}_{cdom}$ along the SGTs was positively and linearly correlated with a_{cdom} (Fig. 4a), consistent with previous findings (Xie et al., 2009; Stubbins et al., 2011). $\bar{\Phi}_{cdom}$ data from the MS and CB covered a narrow a_{cdom} range (0.07–0.33 m^{-1} at 412 nm) and were rather scattered. The mean of the surface water $\bar{\Phi}_{cdom}$ data essentially followed the SGTs' regression line while DCM's mean $\bar{\Phi}_{cdom}$ was well (60 %) above it. Unlike $\bar{\Phi}_{cdom}$, $\bar{\Phi}_p$ did not show significant relationships with particulate optical parameters such as a_p, a_{phy}, and the $a_{phy} : a_p$ ratio (data not shown), suggestive of more complex mechanisms controlling particle-based CO photoproduction. We then divided the $\bar{\Phi}_p$ dataset into five subsets: the SGTs, the surface of the MS, the DCM of the MS, the surface of the CB, and the DCM of the CB. The means of $\bar{\Phi}_p$ calculated from these individual subsets were found to increase exponentially with the $a_{phy,412} : a_{p,412}$ ratio, albeit with relatively large error bars (Fig. 4b). Hence, the content of phytoplankton-derived organic matter could partly regulate the efficiency of CO photoproduction from particles.

BGD
9, 16161–16211, 2012

It should be pointed out that KCN used for poisoning samples (see Sect. 2.3), though transparent to UV and visible light, suppresses CO photoproduction (Xie and Zafiriou, 2009). Previous tests indicated that addition of 43.0 µmol l^{-1} KCN to filtered seawater samples from a wide range of latitudes decreased CO photoproduction by 25 %–36 % (H. Xie and O. C. Zafiriou, unpublished data). In the present study we reduced the KCN dose to 4.3 µmol l^{-1}, which greatly mitigated the KCN effect on CO photoproduction while was still sufficient to eradicate microbial CO uptake over the irradiation periods adopted. The KCN inhibition of CO production in filtered samples was on average 6.5 % (range: 3.5 %–16.0 %, $n = 20$) in the UV domain and negligible in the visible domain. A limited number of tests on unfiltered samples, in which microbial CO consumption was negligible without poisoning, showed a similar suppression of CO production by KCN. No correction was made for the KCN effect since it was generally small and not all samples were evaluated.

3.3 Photoreactivity of CDOM and particles

The decrease in surface water $\bar{\Phi}_{cdom}$ from the estuary to open ocean (Fig. 3) suggests that CDOM photoreactivity with respect to CO photoproduction declined seaward. Such a decay of CDOM photoreactivity could be attributed to a progressively increasing proportion of marine CDOM with distance from land and/or structural modifications associated with photobleaching when CDOM was transported across the MS. Marine CDOM is generally less photoreactive than its terrigenous counterpart (Zepp, 2003) and photobleaching reduces CDOM's CO photoproduction efficiency (Zhang et al., 2006). The photoreactivity of particles in surface water, in terms of $\bar{\Phi}_p$, augmented from the estuary to offshore, displaying an inverse tendency to the CDOM photoreactivity (Fig. 3). Hence, marine particles appeared more photoreactive than riverine particulates. Notably, CDOM and particles both exhibited higher photoreactivities at the DCM than at the surface (Fig. 3). The higher CDOM photoreactivity at the DCM might be linked to the fact that the DCM layer carried CDOM characteristic of the Pacific summer water (Matsuoka et al., 2011, 2012) and that underwater CDOM was shielded from

BGD
9, 16161–16211, 2012

photobleaching. Concerning the particulate phase, fresher cells and/or higher organic contents (more on this point below) within the DCM could make the particles there be more photoreactive, since $\bar{\Phi}_p$ increased with the $a_{phy} : a_p$ ratio (Fig. 4b). The particulate photoreactivity was far below the CDOM photoreactivity in the estuary but the sequence reversed on the MS and in the CB (Fig. 3). This observation of higher particulate photoreactivity for the Arctic shelf and offshore waters is consistent with the results of a previous study using mid-latitude coastal and open waters (Xie and Zafiriou, 2009).

It should be pointed out that the particulate photoreactivity discussed above refers to the bulk particulate matter without differentiating the organics from inorganics. As the relative content of suspended minerals often varied considerably among different sampling stations, particularly along the SGTs, the effect of minerals on the POM-based photoreactivity is expected to differ as well. We used the following approach to retrieve the POM-based CO AQY, Φ_{pom}, for the SGT stations. First, a sensitivity analysis was conducted to evaluate how the $\Phi_{pom} : \Phi_p$ ratio changes with the $a_{pom} : a_p$ ratio (where a_{pom} is the absorption coefficient of POM in m^{-1}) for each of the SGT stations. Φ_{pom} was calculated in the same manner as that for Φ_p using Eqs. (3)–(9). The $a_{pom} : a_p$ ratio increased from 0.1 to 1 with intervals of 0.1; Φ_{pom} equals Φ_p when the $a_{pom} : a_p$ ratio is unity. For a given $a_{pom} : a_p$ ratio at a specific wavelength (here we chose 412 nm), the $\Phi_{pom} : \Phi_p$ ratio was found to be essentially constant across the entire wavelength range of interest (280 nm–600 nm; within 2.0 %) and for all stations tested (within 3 %). The $\Phi_{pom} : \Phi_p$ and $\bar{\Phi}_{pom} : \bar{\Phi}_p$ ratios can be fitted to an quasi-exponential function of the $a_{pom} : a_p$ ratio (Fig. 5). Thus, the spectra of Φ_{pom} can be obtained according to the $a_{pom} : a_p$ ratio. Second, a_{pom} was calculated as $a_{phy} + a_0$, where a_0 (m^{-1}) represents the organic particle absorption not removed by the methanol treatment (see Sect. 2.4). Following the method of Moate et al. (2012), we derived a_0 as the intercept of a linear regression of a_{nap} against the concentration of suspended minerals, M ($g\,m^{-3}$); the slope of this regression is the mass-specific absorption coefficient of the minerals, a^*_M ($m^2\,g^{-1}$). M was calculated as the difference between the total suspended particulate matter (SPM) and POM. POM was estimated as 2.6 times the particulate

BGD
9, 16161–16211, 2012

organic carbon (POC) (Copin-Montégut, 1980). Martin et al. (1993) adopted a similar POM : POC ratio for the Lena River estuary on the Siberian Arctic shelf. The a_{nap}, SPM, and POC data, separately collected by Doxaran et al. (2012) from the SGTs during the same cruise, were used to perform the regression of a_{nap} on M (since our own study did not measure SPM and POC). The derived a_0 and a^*_M as a function of wavelength are shown in Fig. 6. The spectral shape and values of a^*_M obtained in the present study are comparable to those in the Conwy and Mersey estuaries of the Irish Sea (Moate et al., 2012). They also mimic the a^*_M spectra of Saharan dusts in red rain collected at the Mediterranean coast in France (Babin and Stramski, 2004). Finally, knowing a_{pom} gives the $a_{pom} : a_p$ ratios of our SGT samples and hence their $\Phi_{pom} : \Phi_p$ ratios, from which Φ_{pom} can be computed since Φ_p is known (see Sect. 3.2).

The $a_{pom} : a_p$ ratio gradually ascended with salinity in the relatively fresh zone (salinity < 20), followed by a surge with further rising salinity (Fig. 7a), demonstrating an increasing proportion of particulate chromophoric organic matter toward the sea. Sta. 693 (salinity: 15.00) was an exception whose $a_{pom} : a_p$ ratio was lowest and hence temporarily reversed the upward trend. The a_{pom} in the SGT samples contributed on average 32 % to a_p at 412 nm (range: 13 %–71 %; median: 22 %). As expected, the $\bar{\Phi}_{pom} : \bar{\Phi}_p$ ratio was always greater than unity and roughly mirrored the pattern of the $a_{pom} : a_p$ ratio with respect to salinity (Fig. 7a). The $\bar{\Phi}_{pom} : \bar{\Phi}_p$ ratio averaged 6.2 and spanned from 1.9 to 12.2. Despite Φ_p being lower than Φ_{cdom} for most SGT stations (Table 3 and Fig. 3), Φ_{pom} mostly surpassed Φ_{cdom} often by large extents (Fig. 7a). The mean $\bar{\Phi}_{pom} : \bar{\Phi}_{cdom}$ ratio reached 2.7 with a range from 1.0 to 4.8. Figure 7b displays an example of the Φ_{pom} spectrum and its parallel Φ_{cdom} and Φ_p spectra (Sta. 697). Although Φ_p was lower than Φ_{cdom} essentially over the entire spectral range, Φ_{pom} lied above Φ_{cdom} throughout the interested wavelengths. POM was thus more photoreactive than CDOM in the estuary. Because a_{nap} showed no significant relationship to the mineral concentration in the shelf and offshore water samples (data not shown), the a_0 and a^*_M of these samples could not be obtained from the regression method described above, thereby disabling us to derive their a_{pom} and Φ_{pom}. However, since the $a_{phy} : a_p$

BGD
9, 16161–16211, 2012

ratio in shelf and offshore waters was high (Table 2) and the $a_{pom} : a_p$ ratio should be even higher, $\bar{\Phi}_{pom}$ of these samples was estimated to be on average < 1.3 times their $\bar{\Phi}_p$, or $< 3.73 \times 10^{-6}$ in absolute value. This value is 9 % lower than the average $\bar{\Phi}_{pom}$ of the SGT samples. Hence, vascular plant-dominated terrigenous POM discharged from the Mackenzie River was similarly or even more photoreactive, with respect to CO photoproduction, as compared to the largely algae-derived marine POM produced in the open Beaufort Sea. Employing lipid biomarkers to trace the degradation state of organic matter, Rontani et al. (2012) observed a strong autoxidative processing of terrigenous POM in the Mackenzie River and its neighboring shelf and suggested that photochemistry is involved in this process. Our result supports these authors' proposition from a different perspective. The large differences in photoreactivities between POM and bulk particulate matter revealed in the present study highlight the necessity of separating the optical contribution of inorganic constituents from that of organic materials, particularly for mineral-rich waters, when studying POM photochemistry. Readers are referred to Bowers and Binding (2006) and Moate et al. (2012) for recent advances in characterization of the optical properties of suspended minerals, including their absorption spectra, in marine waters.

Several studies have reported that POM can be photochemically transformed to DOM, including CDOM (Anesio et al., 1999b; Mayer et al., 2009; Pisani et al., 2011). POM-based CO photoproduction could thus arise directly from POM itself or indirectly from POM-derived CDOM. The current study does not aim to distinguish between the two pathways. We, however, did monitor the effect of irradiation on CDOM in certain particle-containing samples and found no substantial production of new CDOM over the relatively short periods of light exposure adopted in our experiments (mostly < 3 h) (data not shown). CO photoproduction from newly produced CDOM, if any, should therefore not be the primary process responsible for the particle-driven CO photoproduction observed in this study.

BGD
9, 16161–16211, 2012

3.4 Action spectra of CO photoproduction

The action spectrum of CO photoproduction at the sea surface, $\Lambda_{0,\lambda}$ (mol CO m^{-3} h^{-1} nm^{-1}), was calculated using Eq. (11),

$$\Lambda_{0,\lambda} = Q_{0,\lambda} \times a_{\lambda} \times \Phi_{\lambda} \quad (11)$$

where $Q_{0,\lambda}$ is defined in Eq. (10) and a_{λ} and Φ_{λ} denote $a_{\mathrm{cdom},\lambda}$ and $\Phi_{\mathrm{cdom},\lambda}$ for CDOM and $a_{\mathrm{p},\lambda}$ and $\Phi_{\mathrm{p},\lambda}$ for particles (Fig. 8a, b). Both CDOM and particle action spectra were characterized by a non-Gaussian style with the peak response located at 330 nm and a long tail in the visible (Fig. 8c, d). While the particle action spectra were far below the CDOM's in the UV range (290–400 nm), the former were conspicuously above the latter across most of the visible section (> 400 nm), leading to a flatter transition from the UV to visible in the particle action spectra. Averaged on action spectra of all surface water samples, UV-B (280–320 nm) contributed 23 % (range: 18 %–28 %), UV-A (320–400 nm) 71 % (range: 68 %–74 %), and the visible (400–600 nm) 6 % (range: 5 %-9 %) to Λ_0 of CDOM integrated over 290–600 nm. The spectral contributions to the wavelength-integrated Λ_0 of particles were: 14 % (range: 4 %–26 %) from UVB, 64 % (range: 45 %–70 %) from UVA and 23 % (range: 5 %–52 %) from the visible. The mean percent contribution from the visible displayed little variations across the three sub-regions but was higher for DCM samples (36 %) than for surface samples (23 %). The visible component in the particle action spectra was on average four times that in the CDOM action spectra.

Depth-integrated action spectra in the photic zone, $\Lambda_{\mathrm{col},\lambda}$ (mol CO m^{-2} h^{-1} nm^{-1}), were computed using Eq. (12),

$$\Lambda_{\mathrm{col},\lambda} = Q_{0,\lambda} \times (a_{\lambda}/a_{\mathrm{t},\lambda}) \times \Phi_{\lambda} \quad (12)$$

Here $a_{\mathrm{t},\lambda}$ is the total absorption coefficient in the water column, i.e. the sum of $a_{\mathrm{cdom},\lambda}$, $a_{\mathrm{p},\lambda}$, and $a_{\mathrm{w},\lambda}$ in the euphotic zone. Surface water AQY and absorption values were assumed for the entire euphotic zone, which is a reasonable postulation since the

BGD
9, 16161–16211, 2012

euphotic zone was generally shallower than the surface mixed layer (Taalba et al., unpublished data). Like the surface action spectra, the peak-response wavelengths of the water column action spectra also occurred at 330 nm but their patterns substantially shifted to the visible, particularly for the particle spectra (Fig. 8e, f). Particle action spectra for DCM samples were an exception which lacked the typical, sharp response peak and was characterized by a broad elevation, instead (Fig. 8f). This pattern is consistent with the presence of perceptible shoulders in the Φ_p spectra over the visible band for DCM samples (Fig. 2d, e). Averaged on action spectra of all surface water samples, UV-B, UV-A, and the visible accounted for, respectively, 12 % (range: 9 %–16 %), 67 % (range: 63 %–70 %), and 21 % (range: 14 %–28 %) of CDOM's Λ_{col} integrated from 290 nm–600 nm and 5 % (range: 1 %–15 %), 44 % (range: 26 %–71 %), and 51 % (range: 15 %–73 %) of particles' Λ_{col}. Compared to the surface action spectra, the percent contributions from the visible in the water column action spectra increased for both CDOM and particles but the one for particles went up far more. The difference in the spectral contributions between the surface and water column action spectra arose from the fact that the UV radiation was more rapidly attenuated than the visible light during their transmission in the water column (Fig. 9a).

To examine the effect of varying spectral light propagation on the depth dependence of CO photoproduction in the water column, we modeled the vertical distribution of spectral solar photon fluxes using Eq. (13),

$$Q_{z,\lambda} = Q_{0,\lambda} \times \exp(-k_{d,\lambda} \times z) \quad (13)$$

where $Q_{z,\lambda}$ is the spectral photon flux at depth z (m) and $k_{d,\lambda}$ the diffuse attenuation coefficient (m^{-1}) (Doxaran et al., 2012). The action spectrum at depth z, $\Lambda_{z,\lambda}$ (mol CO m^{-3} h^{-1} nm^{-1}), is given by

$$\Lambda_{z,\lambda} = Q_{z,\lambda} \times a_\lambda \times \Phi_\lambda \quad (14)$$

$Q_{z,\lambda}$ and $\Lambda_{z,\lambda}$ for the UV-B, UV-A and visible bands were calculated by integration over the relevant wavelength ranges. Clearly, the visible light and visible-driven CO

BGD
9, 16161–16211, 2012

production penetrated much deeper than their UV-B and UV-A counterparts (Fig. 9a–c). Consequently, the relative contribution of the visible to full-spectrum (290–600 nm) CO production increased with depth for both CDOM and particles (Fig. 9d). Concerning the full spectrum-integrated Λ_z, the ratio of particles to CDOM rose from 4 % at the surface to 38 % at the base of the euphotic zone (Fig. 9e), due evidently to the dominance of $\Phi_{p,\lambda}$ over $\Phi_{cdom,\lambda}$ at the visible wavelengths (Fig. 2).

3.5 Modeling CO photoproduction

CO photoproduction rates from CDOM and particles were modeled at each station for the sampling season of August 2009. The production rates at the surface (0 m), P_0 (μmol CO m^{-3} d^{-1}), and in the euphotic zone (depth-integrated), P_{col} (μmol CO m^{-2} d^{-1}), were calculated using Eqs. (15) and (16), respectively,

$$P_0 = \int_{290}^{600} Q_{0-,\lambda} \times a_\lambda \times \Phi_\lambda \times d\lambda \quad (15)$$

$$P_{col} = \int_{290}^{600} Q_{d0-,\lambda} \times (a_\lambda / a_{t,\lambda}) \times \Phi_\lambda \times d\lambda \quad (16)$$

P_0, P_{col}, a_λ, and Φ_λ denote $P_{cdom,0}$ and $P_{p,0}$, $P_{cdom,col}$ and $P_{p,col}$, $a_{cdom,\lambda}$ and $a_{p,\lambda}$, and $\Phi_{cdom,\lambda}$ and $\Phi_{p,\lambda}$ for CDOM and POM, respectively. $Q_{0-,\lambda}$ is the scalar photon flux just beneath the surface (mol photons m^{-2} d^{-1} nm^{-1}) and $a_{t,\lambda}$ the sum of $a_{cdom,\lambda}$, $a_{p,\lambda}$, and $a_{w,\lambda}$ in the water column. $Q_{0-,\lambda}$ was estimated as 1.3 times the downwelling photon flux ($Q_{d0-,\lambda}$) (Gordon, 1989). $Q_{d0-,\lambda}$ was simulated using the Santa Barbara DISORT Atmospheric Radiative Transfer (SBDART) software developed by Ricchiazzi et al. (1998) at 3 h intervals, taking into account of the cloud cover and ozone conditions. Major factors

BGD
9, 16161–16211, 2012

influencing solar incident irradiance, such as cloud fraction, cloud optical thickness, and ozone abundance were obtained from the International Satellite Cloud Climatology Project (ISCCP, http://isccp.giss.nasa.gov/products/browsed2.html). Eqs. (15) and (16) employed surface water a_λ and Φ_λ and assumed vertical uniformity of the two parameters in the euphotic zone. Areal CO photoproduction in ice-free water, $\sum P_{col}$, was calculated separately for the MRE, MS, and CB by multiplying the mean P_{col} by the open water area for each sub-region. Demarcation of the three sub-regions is described in Fig. 1. Daily sea ice cover data were provided by the US National Snow and Ice Data Center (NSIDC, http://nsidc.org/)

Both $P_{cdom,0}$ and $P_{p,0}$ reached maxima, 239 µmol CO m^{-3} d^{-1} and 126 µmol CO m^{-3} d^{-1}, at the most nearshore Sta. 697, in line with the highest a_{cdom} and a_p observed at this locality (see Sect. 3.1). The minimum $P_{cdom,0}$ (2.4 µmol CO m^{-3} d^{-1}) and $P_{p,0}$ (0.09 µmol CO m^{-3} d^{-1}) occurred, respectively, at the offshore Sta. 320 and Sta. 220 having low CDOM and particle abundances. The $P_{p,0} : P_{cdom,0}$ ratio was highest at Sta. 697 (0.53) and lowest (0.03) at Sta. 220 and Sta. 380, conforming to the parallel high (4.1) and low (0.10) $a_p : a_{cdom}$ ratios. The maximum $P_{cdom,col}$ (20 µmol CO m^{-2} d^{-1}) and $P_{p,col}$ (6.7 µmol COß, m^{-2} d^{-1}) were found at Sta. 694 and Sta. 697, respectively, while the minimum $P_{cdom,col}$ (6.8 µmol CO m^{-2} d^{-1}) and $P_{p,col}$ (0.3 µmol CO m^{-2} d^{-1}) were both present at Sta. 220. Like the $P_{p,0} : P_{cdom,0}$ ratio, the $P_{p,col} : P_{cdom,col}$ ratio was also highest at Sta. 697 (0.73) and lowest at Sta. 220 (0.04).

Table 4 summarizes the means of modeled CO production rates and other related parameters for each sub-region. $P_{cdom,0}$, $P_{p,0}$, and the $P_{p,0} : P_{cdom,0}$ ratio all decreased from the estuary to the shelf to the basin, which evolved in the same manner as a_{cdom}, a_p, and the $a_p : a_{cdom}$ ratio, respectively (Table 2). $P_{cdom,col}$ for the shelf was comparable to that for the basin but 27 % lower than that for the estuary. $P_{p,col}$ declined from nearshore to offshore. The $P_{p,col} : P_{cdom,col}$ ratios for the estuary and shelf were similar and almost 2.5 times of that for the basin. Because of widening open water area seaward, $\sum P_{cdom,col}$ augmented from the estuary to the shelf to the basin, contrary to

BGD
9, 16161–16211, 2012

the $P_{cdom,col}$ tendency. The combination of relatively high particle abundance and large open water area rendered the MS to possess the highest $\sum P_{p,col}$. The total CO photoproduction in the entire study area in August 2009 amounted to 60×10^6 mol, of which 14 % was produced by POM photodegradation.

Note that the particulate to CDOM CO photoproduction ratios reported in Table 4 were arithmetic averages of these ratios for individual stations within each sub-region. The individual CO production ratios were based on the corresponding individual $a_p : a_{cdom}$ ratios measured. Because of limited spatial coverage by the sampling stations, snapshots of the $a_p : a_{cdom}$ ratio might not be representative of the entire sub-region in question. We therefore also evaluated $P_{p,col}$ and $P_{cdom,col}$ using monthly averaged remote sensing-derived a_t (Bélanger, 2006) and $a_{cdom} : a_t$ ratios (Bélanger et al., 2008), from which a_p and a_{cdom} (hence $a_p : a_{cdom}$ ratios) can be calculated since $a_t = a_p + a_{cdom} + a_w$ and a_w is known (Buiteveld et al., 1994; Pope and Fry, 1997). The a_p, a_{cdom} and $a_p : a_{cdom}$ ratio in the present study were obtained from the remote sensing-based a_{cdom} and $a_{cdom} : a_t$ ratios published by Xie et al. (2012, their Table 3). The $P_{p,col}$, $P_{cdom,col}$, and $P_{p,col} : P_{cdom,col}$ ratios derived from ocean color imaging are shown in Table 5. In addition to the sampling month (August), estimates were also made for other months, assuming seasonally constant $\Phi_p : \Phi_{cdom}$ ratios (Table 5). The satellite-derived $P_{p,col} : P_{cdom,col}$ ratio in August was similar to the individual stations-based ratio for the MS (including MRE) but the former was nearly twice the latter for the CB due to the much higher $a_p : a_{cdom}$ ratio from remote sensing. The $P_{p,col} : P_{cdom,col}$ ratio generally decreased from April (MS: 0.40; CB: 0.48) to September (MS: 0.15; CB: 0.13) and followed a similar pattern for the $a_p : a_{cdom}$ ratio, underscoring the importance of the POM versus CDOM absorption seasonality in controlling the POM- versus CDOM-based CO photoproduction dynamics. The open water area-normalized annual $P_{p,col} : P_{cdom,col}$ ratio reached 0.24 on the MS and 0.17 in the CB. These ratios are within the range reported by Xie and Zafiriou (2009) for mid-latitude coastal and open ocean waters. As the $P_{p,col} : P_{cdom,col}$ ratio is linearly correlated to the $a_p : a_{cdom}$ ratio ($Y = 0.58X - 0.03$,

BGD
9, 16161–16211, 2012

$R^2 = 0.87$, $p < 0.0001$, $n = 12$), it is feasible to extrapolate our results to other ocean areas with known $a_p : a_{cdom}$ ratios.

4 Summary

AQY spectra of CO photoproduction from CDOM and particles were determined using water samples from the Mackenzie estuary, shelf, and Canada Basin. Bulk particulate matter-based CO AQY increased from land to sea, opposite to the trend of CDOM-based CO AQY. Samples from the deep chlorophyll maximum layer displayed higher CO AQY for both particles and CDOM than did surface water samples. CO AQY of bulk particulate matter in shelf and offshore waters exceeded that of CDOM but the reverse held for estuarine water. While CDOM's CO AQY generally increased linearly with CDOM's absorption coefficient, particulate matter's CO AQY, if averaged over suitable sub-divisions of the sampling area, was positively related to the ratio of phytoplankton to total particulate absorption. Excluding the contribution of minerals to the absorption coefficient of the bulk particles, POM-based CO AQY in estuarine water surpassed its CDOM counterpart and was at least comparable to that in shelf and offshore waters. With respect to CO photoproduction, the AQY data demonstrate that (1) riverine CDOM was more photoreactive than CDOM of marine origin; (2) land-derived POM exhibited photoreactivity that was similar to or even higher than marine POM; (3) POM photoreactivity was higher than CDOM photoreactivity, regardless of the origin of the particulate and dissolved organic matter (i.e. terrigenous or marine). The spectral shape of particle-based CO AQY was flatter than that of CDOM-based CO AQY in the visible wavelengths, leading to a continuously increasing proportion of CO produced from particles with depth in the water column. Although depth-integrated CO photoproduction from CDOM was primarily driven by the UV radiation, the visible domain contributed roughly as much as the UV to CO photoproduction from particles. AQY-based coupled optical-photochemical modeling indicates that CO photoproduction from particles in the study area was equivalent to 13–48 % of that from CDOM.

BGD
9, 16161–16211, 2012

Appendix A

List of symbols and abbreviations

Symbol	Meaning	Unit
a	absorption coefficient	m^{-1}
a_0	organic particle absorption coefficient not removed by the methanol treatment	m^{-1}
a_{cdom}	absorption coefficient of CDOM	m^{-1}
a_{nap}	absorption coefficient of non-algal particles	m^{-1}
a_p	absorption coefficient of particles	m^{-1}
a_{phy}	absorption coefficient of phytoplanktonic pigments	m^{-1}
a_{pom}	absorption coefficient of POM	m^{-1}
a_t	absorption coefficient of the sum of a_{cdom}, a_p, and a_w	m^{-1}
a_w	absorption coefficient of pure water	m^{-1}
a^*_M	mass-specific absorption coefficient of minerals	$m^2\,g^{-1}$
A	clearance area of filters for retaining particles	m^2
bb_m	particle backscattering coefficient	m^{-1}
β	path length amplification factor	unitless
k_d	diffuse attenuation coefficient	m^{-1}
λ	wavelength	nm
L	light path length of irradiation cells	m
OD	optical density	unitless
OD_{blank}	optical density of blank GF/F filter	unitless
OD_{cdom}	optical density of CDOM	unitless
OD_f	optical density of particles	unitless

BGD
9, 16161–16211, 2012

Symbol	Meaning	Unit
P_0	CO photoproduction rate at the surface	$\mu mol\,CO\,m^{-3}\,d^{-1}$
$P_{cdom,0}$	CO photoproduction rate at the surface from CDOM	$\mu mol\,CO\,m^{-3}\,d^{-1}$
$P_{p,0}$	CO photoproduction rate at the surface from particles	$\mu mol\,CO\,m^{-3}\,d^{-1}$
P_{col}	depth-integrated CO photoproduction rate in the euphotic zone	$\mu mol\,CO\,m^{-2}\,d^{-1}$
$P_{cdom,col}$	depth-integrated CO photoproduction rate in the euphotic zone from CDOM	$\mu mol\,CO\,m^{-2}\,d^{-1}$
$P_{p,col}$	depth-integrated CO photoproduction rate in the euphotic zone from particles	$\mu mol\,CO\,m^{-2}\,d^{-1}$
$\sum P_{col}$	area-integrated CO photoproduction in the euphotic zone	$mol\,CO\,m^{-2}\,d^{-1}$
$\sum P_{cdom,col}$	area-integrated CO photoproduction in the euphotic zone from CDOM	$mol\,CO\,m^{-2}\,d^{-1}$
$\sum P_{p,col}$	area-integrated CO photoproduction in the euphotic zone from particles	$mol\,CO\,m^{-2}\,d^{-1}$
Φ	CO apparent quantum yield (AQY)	$mol\,CO\,(mol\,photons)^{-1}$
Φ_{cdom}	AQY from CDOM	$mol\,CO\,(mol\,photons)^{-1}$
Φ_p	AQY from particles	$mol\,CO\,(mol\,photons)^{-1}$
Φ_{pom}	AQY from POM	$mol\,CO\,(mol\,photons)^{-1}$
Φ_t	AQY from CDOM plus particles	$mol\,CO\,(mol\,photons)^{-1}$
$\bar{\Phi}$	solar irradiance spectrum-weighted mean Φ (290–600 nm)	$mol\,CO\,(mol\,photons)^{-1}$

BGD
9, 16161–16211, 2012

Symbol	Meaning	Unit
$\bar{\Phi}_{cdom}$	solar irradiance spectrum-weighted mean Φ (290–600 nm) for CDOM	mol CO (mol photons)$^{-1}$
$\bar{\Phi}_{p}$	solar irradiance spectrum-weighted mean Φ (290–600 nm) for particles	mol CO (mol photons)$^{-1}$
$\bar{\Phi}_{pom}$	solar irradiance spectrum-weighted mean Φ (290–600 nm) for POM	mol CO (mol photons)$^{-1}$
$\bar{\Phi}_{t}$	solar irradiance spectrum-weighted mean Φ (290–600 nm) for CDOM plus particles	mol CO (mol photons)$^{-1}$
Q	photon flux just below the frontal quartz window	mol photons m^{-2} s^{-1} nm^{-1}
Q_a	photons absorbed by CDOM, particles and water	mol photons m^{-2} s^{-1} nm^{-1}
Q_0	modeled surface solar photon fluxes	mol photons m^{-2} h^{-1} nm^{-1}
Q_{0-}	scalar photon flux just beneath the sea surface	mol photons m^{-2} h^{-1} nm^{-1}
Q_{d0-}	downwelling photon flux just beneath the sea surface	mol photons m^{-2} h^{-1} nm^{-1}
Q_z	photon flux at depth z (m)	mol photons m^{-2} h^{-1} nm^{-1}
S	cross-section of the irradiation cells	m^{-2}
V	filtered volume of seawater through GF/F filters	m^{3}
Λ	surface CO action spectrum	mol CO m^{-3} h^{-1} nm^{-1}
Λ_{col}	depth-integrated CO action spectrum	mol CO m^{-2} h^{-1} nm^{-1}

BGD
9, 16161–16211, 2012

Abbreviation	Meaning
AQY	apparent quantum yield
CB	Canada Basin
CDOM	chromophoric dissolved organic matter
Chl *a*	chlorophyll *a*
DCM	deep chlorophyll maximum
MRE	Mackenzie River estuary
MS	Mackenzie Shelf
POM	particulate organic matter
SGT-E	salinity gradient transect-east channel
SGT-W	salinity gradient transect-west channel
SPM	suspended particulate matter
UVA	Ultraviolet-A (320–400 nm)
UVB	Ultraviolet-B (290–320 nm)

Acknowledgements. We thank D. Doxaran and J. Ehn for providing the POC, SPM, and backscattering data. We are grateful to M. Babin, the chief scientist of the *CCGS Amundsen* cruise and the principal investigator of the Malina program. This study was supported by grants from NSERC (Natural Sciences and Engineering Research Council) and conducted as part of the Malina Scientific Program funded by ANR (Agence nationale de la recherche), INSU-CNRS (Institut national des sciences de l'univers – Centre national de la recherche scientifique), CNES (Centre national d'études spatiales) and ESA (European Space Agency). GS received graduate scholarships from ISMER (Institut des sciences de la mer de Rimouski) and FRQNT (Fonds de recherche du Québec – Nature et technologies).

BGD
9, 16161–16211, 2012

References

Anesio, A. M., Tranvik, L. J., and Granéli, W.: Production of inorganic carbon from aquatic macrophytes by solar radiation, Ecology, 80, 1852–1859, 1999a.

Anesio, A. M., Denward, C. M. T., Tranvik, L. J., and Granéli, W.: Decreased bacterial growth on vascular plant detritus due to photochemical modification, Aquat. Microb. Ecol., 17, 159–165, 1999b.

Babin, M. and Stramski, D.: Variations in the mass-specific absorption coefficient of mineral particles suspended in water, Limnol. Oceanogr., 49, 756–767, 2004.

Babin, M., Stramski, D., Ferrari, G. M., Claustre, H., Bricaud, A., Obolensky, G., and Hoepffner, N.: Variations in the light absorption coefficients of phytoplankton, nonalgal particles, and dissolved organic matter in coastal waters around Europe, J. Geophy. Res., 108, 3211, doi:10.1029/2001JC000882, 2003.

Bélanger, S.: Response of light-related carbon fluxes in the Arctic Ocean to climate change: quantification and monitoring of dissolved organic matter photo-oxidation in the Beaufort Sea using satellite remote sensing, PhD. thesis, Université Pierre et Marie Curie (UPMC – Paris XI), Paris, France, 2006.

Bélanger, S., Xie, H., Krotkov, N., Larouche, P., Vincent, W. F., and Babin, M: Photomineralization of terrigenous dissolved organic matter in Arctic coastal waters from 1979 to 2003: interannual variability and implications of climate change, Global Biogeochem. Cy., 20, GB4005, doi:10.1029/2006GB002708, 2006.

Bélanger, S., Babin, M., and Larouche, P.: An empirical ocean color algorithm for estimating the contribution of chromophoric dissolved organic matter to total light absorption in optically complex waters. J. Geophys. Res. 113, C04027, doi:10.1029/2007JC004436, 2008.

Benner, R. and Biddanda, B.: Photochemical transformations of surface and deep marine dissolved organic matter: effects on bacterial growth, Limnol. Oceanogr. 43, 1373–1378, 1998.

Benner, R. and Kaiser, K.: Biological and photochemical transformations of lignin phenols and amino acids in riverine dissolved organic matter, Biogeochemistry, 102, 209–222, 2010.

Benner, R., Louchouarn, P., and Amon, R. M. W.: Terrigenous dissolved organic matter in the Arctic Ocean and its transport to surface and deep waters of the North Atlantic, Global Biogeochem. Cy., 19, GB2025, doi:10.1029/2004GB002398, 2005.

BGD
9, 16161–16211, 2012

Blough, N. V. and Zepp, R. G.: Reactive oxygen species in natural waters, in: Active Oxygen in Chemistry, edited by: Foote, C. S., Pacentine, J. S., Greenberg, A., and Liebman, J. F., Chapman and Hall, New York, 280–333, 1995.
Brimblecombe, P.: The global sulfur cycle, in: Biogeochemistry: Treatise on Geochemistry, edited by: Schlesinger, W. H., Elsevier Ltd., 645–682, 2003.
Bowers, D. G. and Binding, C. E.: The optical properties of mineral suspended particles: a review and synthesis, Estuar. Coast. Shelf S., 67, 219–230, 2006.
Buiteveld, H., Hakvoort, J. M. H., and Donze, M.: The optical properties of pure water, in: SPIE Proceeding on Ocean Optics Pt. XII, edited by: Jaffe, J. S., The Society of Photo-Optical Instrumentation Engineers, 174–183, 1994.
Bushaw, K. L., Zepp, R. G., Tarr, M. A., Schulz-Jander, D., Bourboniere, R. A., Hodson, R. E., Miller, W. L., Bronk, D. A., and Moran, M. A.: Photochemical release of biologically labile nitrogen from aquatic dissolved organic matter, Nature, 381, 404–407, 1996.
Conrad, R., Seiler, W., Bunse, G., and Giehl, H.: Carbon monoxide in seawater (Atlantic Ocean), J. Geophy. Res., 87, 8839–8852, 1982.
Copin-Montégut, G.: Matières en suspension dans les eaux de mer: répartition composition chimique, origine et evolution, Thèse d'état, Université Pierre et Marie Curie Paris IV, 173 pp., 1980.
Dittmar, T. and Kattner, G.: The biogeochemistry of the river and shelf ecosystem of the Arctic Ocean: a review, Mar. Chem., 83, 103–120, 2003.
Doxaran, D., Ehn, J., Bélanger, S., Matsuoka, A., Hooker, S., and Babin, M.: Optical characterisation of suspended particles in the Mackenzie River plume (Canadian Arctic Ocean) and implications for ocean colour remote sensing, Biogeosciences, 9, 3213–3229, doi:10.5194/bg-9-3213-2012, 2012.
Estapa, M. L. and Mayer, L. M.: Photooxidation of particulate organic matter, carbon/oxygen stoichiometry, and related photoreactions, Mar. Chem., 122, 138–147, 2010.
Fichot, C. G. and Miller, W. L.: An approach to quantify depth-resolved marine photochemical fluxes using remote sensing: application to carbon monoxide (CO) photoproduction, Remote Sens. Environ., 114, 1363–1377, 2010.
Fioletov, V. E., Kimlin, M. G., Krotkov, N., McArthur, L. J. B., Kerr, J. B., Wardle, D. I., Herman, J. R., Meltzer, R., Mathews, T. W., and Kaurola, J.: UV index climatology over the United States and Canada from ground-based and satellite estimates, J. Geophys. Res., 109, D22308, doi:10.1029/2004JD004820, 2004.

BGD
9, 16161–16211, 2012

Flato, G. M., Boer, G. J., Lee, W. G., McFarlane, N. A., Ramsden, D., Reader, M. C., and Weaver, A. J.: The Canadian Centre for climate modeling and analysis global coupled model and its climate, Clim. Dynam., 16, 451–467, 2000.
Forest, A., Sampei, M., Hattori, H., Makabe, R., Sasaki, H., Fukuchi, M., Wassmann, P., and Fortier, L.: Particulate organic carbon fluxes on the slope of the Mackenzie Shelf (Beaufort Sea): physical and biological forcing of shelf-basin exchange, J. Mar. Syst., 68, 39–54, 2007.
Goñi, M. A., Yunker, M. B., Macdonald, R. W., and Eglinton, T. I.: The supply and preservation of ancient and modern components of organic carbon in the Canadian Beaufort Shelf of the Arctic Ocean, Mar. Chem., 93, 53–73, 2005.
Gordon, H. R.: Can the Lambert-Beer law be applied to the diffuse attenuation coefficient of ocean water, Limnol. Oceanogr., 34, 1389–1409, 1989.
Gueymard, C. A.: Parameterized transmittance model for direct beam and circumsolar spectral irradiance, Sol. Energy, 71, 325–346, 2001.
Hansell, D. A., Kadko, D., and Bates, N. R.: Degradation of terrigenous dissolved organic carbon in the Western Arctic Ocean, Science, 304, 858–861, 2004.
Holm-Hansen, O., Lorenzen, C. J., Holmes, R. W., and Strickland, J. D.: Fluorometric determination of chlorophyll, J. Cons. Int. Explor. Mer, 30, 3–15, 1965.
Hu, C., Muller-Karger, F. E., and Zepp, R. G.: Absorbance, absorption coefficient, and apparent quantum yield: a comment on common ambiguity in the use of these optical concepts, Limnol. Oceanogr., 47, 1261–1267, 2002.
Johannessen, S. C. and Miller, W. L.: Quantum yield for the photochemical production of dissolved inorganic carbon in seawater, Mar. Chem., 76, 271–283, 2001.
Kettle, A. J.: Diurnal cycling of carbon onoxide (CO) in the upper ocean near Bermuda, Ocean Model., 8, 337–367, 2005.
Kieber, D. J., McDaniel, J. A., and Mopper, K.: Photochemical source of biological substrates in seawater: implications for carbon cycling, Nature, 341, 637–639, 1989.
Kieber, R. J., Hydro, L. H., and Seaton, P. J.: Photooxidation of triglycerides and fatty acids in seawater: implication toward the formation of marine humic substances, Limnol. Oceanogr., 42, 1454–1462, 1997.
Kieber, R. J., Whitehead, R. F., and Skrabal, S. A.: Photochemical production of dissolved organic carbon from resuspended sediment, Limnol. Oceanogr., 51, 2187–2195, 2006.
King, G. M. and Weber, C. F.: Distribution, diversity and ecology of aerobic CO-oxidizing bacteria, Nature Rev. Microbiol., 5, 107–118, 2007.

BGD
9, 16161–16211, 2012

Kirk, J. T. O.: Spectral adsorption properties of natural waters: contribution of the soluble and particulate fractions to light absorption in some inland waters of South-Eastern Australia, Aust. J. Mar. Fresh. Res., 31, 287–296, 1980.

Macdonald, R. W., Carmack, E. C., McLaughlin, F. A., Falkner, K. K., and Swift, J. H.: Connections among ice, runoff and atmospheric forcing in the Beaufort Gyre, Geophy. Res. Lett., 26, 2223–2226, 1999.

Magen, C., Chaillou, G., Crowe, S. A., Mucci, A., Sundby, B., Gao, A., Makabe, R., and Sasaki, H.: Origin and fate of particulate organic matter in the Southern Beaufort Sea–Amundsen Gulf region, Canadian Arctic, Estuar. Coast. Shelf S., 86, 31–41, 2010.

Martin, J. M., Guana, D. M., Elbaz-Poulichet, F., Thomas, A. J., Gordeev, V. V.: Preliminary assessment of the distributions of some trace elements (As, Cd, Cu, Fe, Ni, Pb and Zn) in a pristine aquatic environment: the Lena River estuary (Russia), Mar. Chem., 43, 185–199, 1993.

Matsuoka, A., Hill, V., Huot, Y., Bricaud, A., and Babin, M.: Seasonal variability in the light absorption properties of Western Arctic waters: parameterization of the individual components of absorption for ocean color applications, J. Geophys. Res., 116, C02007, doi:10.1029/2009JC005594, 2011.

Matsuoka, A., Bricaud, A., Benner, R., Para, J., Sempéré, R., Prieur, L., Bélanger, S., and Babin, M.: Tracing the transport of colored dissolved organic matter in water masses of the Southern Beaufort Sea: relationship with hydrographic characteristics, Biogeosciences, 9, 925–940, doi:10.5194/bg-9-925-2012, 2012.

Mayer, L. M., Schick, L. L., Hardy, K. R., and Margaret, L. E.: Photodissolution and other photochemical changes upon irradiation of algal detritus, Limnol. Oceanogr., 54, 1688–1698, 2009.

McLaughlin, F. A., Carmack, E. C., Macdonald, R. W., and Bishop, J. K. B.: Physical and geochemical properties across the Atlantic/Pacific water mass front in the Southern Canadian Basin, J. Geophy. Res., 101, 1183–1197, 1996.

Miller, W. L. and Zepp, R. G.: Photochemical production of dissolved inorganic carbon from terrestrial organic matter: Significance to the oceanic organic carbon cycle, Geophy. Res. Lett., 22, 417–420, 1995.

Miller, W. L., King, D. W., Lin, J., and Kester, D. R.: Photochemical redox cycling of iron in coastal seawater, Mar. Chem., 50, 63–77, 1995.

BGD
9, 16161–16211, 2012

Miller, W. L., Moran, M. A., Sheldon, W. M., Zepp, R. G., and Opsahl, S.: Determination of apparent quantum yield spectra from the formation of biologically labile photoproducts, Limnol. Oceanogr., 47, 343–352, 2002.

Mobley, C. D.: Light and Water: Radiative Transfer in Natural Waters, Academic Press, San Diego, USA, 1994.

Moate, B. D., Bowers, D. G., and Thomas, D. N.: Measurements of mineral particle optical absorption properties in turbid estuaries: intercomparison of methods and implications for optical inversions, Estuar. Coast. Shelf S., 99, 95–107, 2012.

Mopper, K. and Kieber, D. J.: Photochemistry and the cycling of carbon, sulfur, nitrogen and phosphorus, in: Biogeochemistry of Marine Dissolved Organic Matter, edited by: Hansell, D. A. and Carlson, C. A., Academic Press, San Diego, USA, 456–508, 2002.

Moran, M. A. and Miller, W. L.: Resourceful heterotrophs make the most of light in the coastal ocean, Nature Rev. Microbiol., 5, 1–10, 2007.

Nelson, J. R.: Rates and possible mechanism of light-dependent degradation of pigments in detritus derived from phytoplankton, J. Mar. Res., 51, 155–179, 1993.

Opsahl, S. and Benner, R.: Photochemical reactivity of dissolved lignin in river and ocean waters, Limnol. Oceanogr., 43, 1297–1304, 1998.

Opsahl, S., Benner, R., and Amon, R. M. W.: Major flux of terrigenous dissolved organic matter through the Arctic Ocean, Limnol. Oceanogr., 44, 2017–2023, 1999.

Osburn, C. L., Retamal, L., and Vincent, W. F.: Photoreactivity of chromophoric dissolved organic matter transported by the Mackenzie River to the Beaufort Sea, Mar. Chem., 115, 10–20, 2009.

Parsons, T. R., Maita, Y., and Lalli, C. M.: A Manual of Chemical and Biological Methods for Seawater Analysis, Pergamon, New York, 1984.

Pisani, O., Yamashita, Y., and Jaffé, R.: Photo-dissolution of flocculent, detrital material in aquatic environments: contributions to the dissolved organic matter pool, Water Res., 45, 3836–3844, 2011.

Pope, R. M. and Fry, E. S.: Absorption spectrum (380–700 nm) of pure water, 2. Integrating cavity measurements, Appl. Optics, 36, 8710–8723, 1997.

Ricchiazzi, P., Yang, S., and Gautier, C.: SBDART: A Practical Tool for Plane-Parallel Radiative Transfer in the Earth's Atmosphere, available at: http://arm.mrcsb.com/sbdart/html/sbdart-intro.html, 1998.

BGD
9, 16161–16211, 2012

Riggsbee, J. A., Orr, C. H., Leech, D. M., Doyle, M. W., and Wetzel, R. G.: Suspended sediments in river ecosystems: photochemical sources of dissolved organic carbon and adsorptive removal of dissolved iron, J. Geophys. Res., 113, G03019, doi:10.1029/2007JG000654, 2008.

Rontani, J.-F.: Visible light-dependent degradation of lipidic phytoplanktonic components during senescence: a review, Phytochem., 58, 187–202, 2001.

Rontani, J.-F., Zabeti, N., and Wakeham, S. G.: Degradation of particulate organic matter in the equatorial Pacific Ocean: biotic or abiotic? Limnol. Oceanogr., 56, 333–349, 2011.

Rontani, J.-F., Charriere, B., Petit, M., Vaultier, F., Heipieper, H. J., Link, H., Chaillou, G., and Sempéré, R.: Degradation state of organic matter in surface sediments from the Southern Beaufort Sea: a lipid approach, Biogeosciences, 9, 3513-3530, doi:10.5194/bg-9-3513-2012, 2012.

Röttgers, R. and Gehnke, S.: Measurement of light absorption by aquatic particles: improvement of the quantitative filter technique by use of an integrating sphere approach, Appl. Optics, 51, 1336–1351, 2012.

Shank, G. C., Evans, A., Yamashita, Y., Jaffé, R.: Solar radiation–enhanced dissolution of particulate organic matter from coastal marine sediments, Limnol. Oceanogr., 56, 577–588, 2011.

Stedmon, C. A., Amon, R. M. W., Rinehart, A. J., and Walker, S. A.: The supply and characteristics of colored dissolved organic matter (CDOM) in the Arctic Ocean: Pan Arctic trends and differences, Mar. Chem., 124, 108–118, 2011.

SooHoo, J. B. and Kiefer, D. A.: Vertical distribution of phaeopigments-I I. Rates of production and kinetics of photooxidation, Deep-Sea Res. Pt. I, 29, 1553–1563, 1982.

Stroeve, J., Serreze, M., Drobot, S., Gearheard, S., Holland, M., Maslanik, J., Meier, W., Scambos, T.: Arctic sea ice extent plummets in 2007, Eos T. Am. Geophys. Un., 89, 13–14, doi:10.1029/2008EO020001, 2008.

Stubbins, A., Uher, G., Kitidis, V., Law, C. S., Upstill-Goddard, R. C., and Woodward, E. M. S.: The open-ocean source of atmospheric carbon monoxide, Deep-Sea Res. Pt. II, 53, 1685–1694, 2006a.

Stubbins, A., Uher, G., Law, C. S., Mopper, K., Robinson, C., and Upstill-Goddard, R. C.: Open-ocean carbon monoxide photoproduction, Deep-Sea Res. Pt. II, 53, 1695–1705, 2006b.

BGD
9, 16161–16211, 2012

Stubbins, A., Law, C. S., Uher, G., and Upstill-Goddard, R. C.: Carbon monoxide apparent quantum yields and photoproduction in the Tyne estuary, Biogeosciences, 8, 703–713, doi:10.5194/bg-8-703-2011, 2011.

Tarr, M. A., Miller, W. L., and Zepp, R. G.: Direct carbon monoxide photoproduction from plant matter, J. Geophy. Res., 100, 11403–11413, 1995.

Tremblay, J.-É., Simpson, K., Martin, J., Miller, L., Gratton, Y., Barber, D., and Price, N. M.: Vertical stability and the annual dynamics of nutrients and chlorophyll fluorescence in the coastal, southeast Beaufort Sea, J. Geophys. Res., 113, C079S90, doi:10.1029/2007JC004547, 2008.

Vähätalo, A. V. and Zepp, R. G.: Photochemical mineralization of dissolved organic nitrogen to ammonium in the Baltic Sea, Environ. Sci. Technol., 39, 6985–6992, 2005.

Voelker, B. M. and Sedlak, D. L.: Iron reduction by photoproduced superoxide in seawater, Mar. Chem., 50, 93–102, 1995.

Voelker, B. M., Sdelak, D. L., and Zafiriou, O. C.: Chemistry of superoxide radical in seawater: reactions with organic Cu complexes, Environ. Sci. Technol., 34, 1036–1042, 2000.

Williams, W. J. and Carmack, E. C.: Combined effect of wind-forcing and isobaths divergence on upwelling at Cape Bathurst, Beaufort Sea, J. Mar. Res., 66, 645–663, 2008.

White, E. M., Kieber, D. J., Sherrard, J., Miller, W. L., Mopper, K.: Carbon dioxide and carbon monoxide photoproduction quantum yields in the Delaware Estuary, Mar. Chem., 118, 11–21, 2010.

Xie, H. and Zafiriou, O. C.: Evidence for significant photochemical production of carbon monoxide by particles in coastal and oligotrophic marine waters, Geophys. Res. Lett, 36, L23606, doi:10.1029/2009GL041158, 2009.

Xie, H., Andrews, S. S., Martin, W. R., Miller, J., Ziolkowski, L., Taylor, C. D., Zafiriou, O. C.: Walidated methods for sampling and headspace analysis of carbon monoxide in seawater, Mar. Chem., 77, 93–108, 2002.

Xie, H., Bélanger, S., Demers, S., Vincent, W. F., and Papakytiakou, T. N.: Photobiogeochemical cycling of carbon monoxide in the Southeastern Beaufort Sea in spring and autumn, Limnol. Oceanogr., 54, 234–249, 2009.

Xie, H., Bélanger, S., Song, G., Benner, R., Taalba, A., Blais, M., Tremblay, J.-É., and Babin, M.: Photoproduction of ammonium in the southeastern Beaufort Sea and its biogeochemical implications, Biogeosciences, 9, 3047–3061, doi:10.5194/bg-9-3047-2012, 2012.

BGD
9, 16161–16211, 2012

Zafiriou, O. C.: Sunburnt organic matter: biogeochemistry of light-altered substrates, Limnol. Oceanogr. Bulletin, 11, 69–74, 2002.
Zafiriou, O. C., Joussot-Dubien, J., Zepp, R. G., and Zika, R. G.: Photochemistry of natural waters, Environ. Sci. Technol., 18, 358–371, 1984.
Zafiriou, O. C., Andrews, S. S., and Wang, W.: Concordant estimates of oceanic carbon monoxide source and sink process in the Pacific yield a balanced global "blue-water" CO budget, Global Biogeochem. Cy., 17, 1015, doi:10.1029/2001GB001638, 2003.
Zepp, R. G.: Solar UVR and aquatic carbon, nitrogen, sulfur and metals cycles, in: UV Effects in Aquatic Organisms and Ecosystems, edited by: Helbling, E. W. and Zagarese, H., The royal society of chemistry, Cambridge, UK, 137–183, 2003.
Zhang, Y., Xie, H., and Chen, G.: Factors affecting the efficiency of carbon monoxide photoproduction in the St. Lawrence Estuarine system (Canada), Environ. Sci. Technol., 40, 7771–7777, 2006.

BGD
9, 16161–16211, 2012

Table 1. Sampling information along with salinity and water temperature.

Sub-region[a]	Station[b]	Date of Aug 2009	Coordinate Lat., °N	Coordinate Long., °W	Total water depth (m)	Sampling depth (m)[c]	Salinity (°C)	Temp.
SGT-E	392-S	16	70.012	133.522	27	0	27.902	3.2
	394-S	3	69.847	133.492	14	3.5	25.311	7.1
	394-S	16	69.846	133.490	12	0	21.455	7.8
	396-S	16	69.680	133.458	6.3	0	17.267	8.2
SGT-W	691-S	13	69.387	137.792	44	0	23.612	5.2
	692-S	13	69.342	137.594	39	0	22.184	5.9
	693-S	13	69.296	137.398	32	0	15.003	8.8
	694-S	13	69.251	137.202	9.0	0	9.426	9.3
	695-S	13	69.204	137.006	5.0	0	7.042	9.3
	697-S	13	69.125	136.681	1.7	0	0.154	10.3
MS	170-S	7	70.917	128.919	35	3.0	29.009	3.8
	280-S	4	70.869	130.507	38	3.3	27.558	4.8
	280-D	4	70.869	130.507	38	24	31.931	−0.006
	380-S	8	70.393	133.595	62	6.0	27.611	4.1
	380-D	8	70.393	133.595	62	48	31.924	−1.1
	670-S	10	69.797	138.428	173	3.0	23.500	4.0
	780-S	12	70.154	140.801	50	3.0	22.845	3.6
	780-D	12	70.154	140.801	50	30	31.685	−1.1
CB	135-D	20	71.312	127.489	230	60	31.505	−1.3
	220-S	5	70.050	130.945	225	3.0	27.137	−0.8
	220-D	5	70.050	130.945	225	70	31.534	−1.4
	235-D	23	71.728	130.842	611	75	31.965	−1.1
	320-S	9	71.562	133.958	1115	2.8	26.462	−0.7
	320-D	9	71.562	133.958	1115	70	31.546	−1.2
	345-D	15	71.410	132.638	580	60	31.276	−1.0
	430-S	18	71.184	134.748	1300	3.0	26.002	−0.8
	430-D	18	71.184	134.748	1300	65	31.779	−1.1
	460-S	19	70.682	135.891	362	3.0	24.731	−0.06
	460-D	19	70.682	135.891	362	56	31.261	−1.0
	540-S	17	70.756	137.871	1522	3.0	25.292	−0.5
	540-D	17	70.756	137.871	1522	70	31.808	−1.1
	620-S	11	70.674	139.634	1538	3.0	20.751	2.9
	640-S	11	70.334	139.099	550	3.3	21.428	3.3
	760-S	12	70.540	140.785	566	3.1	22.173	0.4
	760-D	12	70.540	140.785	566	70	31.475	−1.1

[a] SGT-E (W) = salinity gradient transect-east (west) channel; MS = Mackenzie Shelf; CB = Canada Basin (see text and Fig. 1 for definitions).
[b] S = surface; D = DCM (deep chlorophyll maximum).
[c] 0 m indicates bucket samples; all other depths indicate Niskin bottle samples.

BGD
9, 16161–16211, 2012

Table 2. Means and ranges (in the parentheses) of salinity, temperature, [Chl *a*], $a_{cdom,412}$, $a_{p,412}$, and the $a_{phy,412} : a_{p,412}$ ratio. Keys in the sub-region column are the same as those in Table 1.

Sub-region	Salinity	Temp. (°C)	[Chl *a*] ($\mu g l^{-1}$)	$a_{cdom,412}$ (m^{-1})	$a_{p,412}$ (m^{-1})	$a_{phy,412} : a_{p,412}$
SGT-E	22.98 (17.27–27.90)	6.4 (3.2–8.2)	1.4 (0.65–2.5)	0.69 (0.12–1.11)	0.22 (0.038–0.36)	0.13 (0.07–0.18)
SGT-W	12.90 (0.15–23.61)	8.6 (5.2–10.3)	1.9 (0.17–3.2)	1.30 (0.39–2.04)	2.65 (0.053–8.40)	0.16 (0.06–0.28)
MS-surface	26.10 (22.85–29.10)	4.1 (3.6–4.8)	2.0 (0.08–7.6)	0.22 (0.13–0.33)	0.076 (0.017–0.26)	0.25 (0.13–0.41)
MS-DCM	31.85 (31.68–31.93)	−0.7 (−0.006 to −1.1)	3.8 (1.3–8.0)	0.17 (0.14–0.22)	0.14 (0.085–0.25)	0.46 (0.22–0.66)
CB-surface	24.25 (20.75–27.14)	0.5 (−0.8–3.3)	0.08 (0.05–0.13)	0.13 (0.07–0.24)	0.012 (0.004–0.026)	0.40 (0.21–0.66)
CB-DCM	31.57 (31.26–31.96)	−1.2 (−1.0 to −1.4)	0.42 (0.12–0.71)	0.14 (0.10–0.23)	0.016 (0.009–0.025)	0.81 (0.56–0.88)

BGD
9, 16161–16211, 2012

Table 3. Fitted parameters for equation $\Phi_\lambda = m_1 \times \exp(m_2/(\lambda + m_3))$ (Eq. 4 in text) for filtered (CDOM) and unfiltered (CDOM plus particles) samples, along with Φ_{330} and $\bar{\Phi}$ for CDOM, CDOM plus particles, and particles. n.d. = not determined.

Station	Filtered sample (CDOM)					Unfiltered sample (CDOM plus particles)					Particles	
	m_1 ($\times 10^{-11}$)	m_2	m_3	Φ_{330} ($\times 10^{-6}$)	$\bar{\Phi}$ ($\times 10^{-6}$)	m_1 ($\times 10^{-11}$)	m_2	m_3	Φ_{330} ($\times 10^{-6}$)	$\bar{\Phi}$ ($\times 10^{-6}$)	Φ_{330} ($\times 10^{-6}$)	$\bar{\Phi}$ ($\times 10^{-6}$)
392-S	0.82	5048.7	21.3	14.3	0.91	78.7	2768.5	−47.0	14.0	1.18	12.9	1.85
394-S	4.02	4573.6	28.1	14.2	1.05	4.25	4219.8	3.53	13.3	0.93	9.74	0.54
396-S	6.74	4282.3	13.1	17.8	1.31	6.81	4074.9	−0.52	16.0	1.15	6.64	0.53
394-ctd	3.29	4371.8	7.48	13.9	0.96	3.73	4367.8	13.8	12.3	0.88	10.1	0.77
691-S	2.25	4410.4	0.67	14.0	0.91	2.18	4641.0	19.6	12.7	0.88	8.69	0.81
692-S	3.64	4362.1	6.90	15.3	1.05	n.d.	n.d.	n.d.	n.d.	n.d.	n.d.	n.d.
693-S	6.77	4390.5	23.2	17.0	1.29	6.87	4091.1	5.18	13.7	1.02	5.84	0.51
694-S	22.2	4346.7	51.1	20.4	1.89	10.9	4051.1	9.15	16.7	1.29	9.64	0.63
695-S	12.9	4814.8	70.3	21.7	1.97	11.0	4047.0	14.8	13.8	1.11	1.82	0.33
697-S	13.7	4861.1	72.5	24.1	2.19	247	1795.0	−118.5	12.0	0.94	5.41	0.52
170-S	1.34	5300.2	50.3	15.1	1.07	5.17	3604.5	−41.5	13.8	0.86	11.2	0.65
280-S	0.72	4754.1	3.93	10.9	0.67	6.98	3946.8	−0.002	10.9	0.82	10.7	1.21
280-D	0.91	6378.6	112.5	16.5	1.30	n.d.	n.d.	n.d.	n.d.	n.d.	n.d.	n.d.
380-S	0.47	5967.6	81.1	9.46	0.69	64.5	2277.4	−83.3	6.59	0.53	3.73	0.37
380-D	1.00	6109.1	93.4	18.5	1.39	1.35	5425.3	63.2	13.2	0.98	7.38	0.63
670-S	1.57	4395.3	−5.80	12.1	0.76	1.64	4645.0	13.1	12.4	0.82	14.3	1.33
780-S	1.57	4782.9	19.8	13.7	0.91	1.66	5078.7	42.7	13.7	0.98	14.1	1.34
780-D	0.86	4988.9	19.0	13.8	0.87	1.57	5073.5	39.7	14.4	1.01	15.2	1.23
135-D	0.52	6039.2	82.9	11.7	0.84	0.59	6496.5	117.5	11.8	0.94	12.3	1.47
220-S	0.35	4566.3	−19.1	8.33	0.46	0.30	4720.0	−7.50	6.91	0.40	5.49	0.33
220-D	0.57	4751.3	5.79	8.02	0.50	0.64	5004.4	24.8	8.56	0.56	12.3	1.28
235-D	0.63	6445.5	110.2	14.3	1.10	0.84	7057.4	155.8	17.1	1.48	25.3	3.38
320-S	0.56	4535.7	−11.9	8.70	0.51	0.35	4914.5	0.82	9.75	0.56	74.2	3.57
320-D	0.58	6210.1	89.2	15.8	1.14	0.80	5710.3	63.5	16.0	1.11	16.2	1.08
345-D	0.66	5328.9	39.4	12.1	0.80	34.8	2991.0	−45.9	13.0	1.00	40.1	3.34
430-S	0.33	5719.3	48.2	12.0	0.76	0.34	6224.4	83.5	11.7	0.82	12.4	1.34
430-D	0.82	7489.0	182.1	18.3	1.67	0.97	6297.7	103.0	20.2	1.54	11.4	1.41
460-S	1.00	5892.0	83.4	16.0	1.19	0.45	5520.2	39.2	14.0	0.89	n.d.	n.d
460-D	0.81	5582.4	54.1	16.6	1.12	0.97	6071.7	91.2	17.6	1.32	19.2	1.91
540-S	0.35	5761.6	52.5	12.3	0.79	39.4	2880.1	−50.2	11.6	0.91	8.29	1.90
540-D	0.88	6218.1	98.2	17.9	1.35	4.45	4713.2	34.7	18.2	1.36	31.4	1.85
620-S	1.41	4816.2	19.5	13.6	0.90	1.45	4872.2	25.0	13.2	0.89	9.80	0.79
640-S	1.51	4770.5	18.3	13.4	0.89	1.53	4756.6	18.6	12.9	0.86	12.4	0.83
760-S	0.86	4396.6	−16.8	10.7	0.63	0.93	4442.3	−12.5	10.5	0.61	n.d.	n.d.
760-D	0.65	6240.1	91.8	17.2	1.25	0.80	6505.6	112.8	19.2	1.48	27.0	2.65

BGD
9, 16161–16211, 2012

Table 4. Arithmetic means (± s.d.) of P, P_{col}, $\sum P_{col}$, and the $a_{p,412} : a_{cdom,412}$ ratio in August 2009 based on individual stations within each sub-region. Keys for MS and CB are the same as those in Table 1.

	MRE[a]	MS	CB
$a_{p,412} : a_{cdom,412}$	0.94	0.39	0.09
	P_0 (μmol m^{-3} d^{-1})		
$P_{cdom,0}$	99 ± 82	11 ± 5	6.5 ± 5
$P_{p,0}$	23 ± 40	1.8 ± 2	0.3 ± 0.2
$P_{p,0} : P_{cdom,0}$	0.23	0.16	0.05
	P_{col} (μmol m^{-2} d^{-1})		
$P_{cdom,col}$	15 ± 3	11 ± 2	11 ± 3
$P_{p,col}$	3.4 ± 2	2.3 ± 2	1.0 ± 0.6
$P_{p,col} : P_{cdom,col}$	0.23	0.21	0.09
	$\sum P_{col}$ (10^3 mol CO d^{-1})		
$\sum P_{cdom,col}$	327 ± 76	571 ± 102	826 ± 239
$\sum P_{p,col}$	75 ± 44	120 ± 87	73 ± 44
Total	403 ± 62	690 ± 96	899 ± 224
Total CO photoproduction in August (10^6 mol CO)			60 ± 12

[a] MRE = Mackenzie River estuary.

BGD
9, 16161–16211, 2012

Table 5. $P_{cdom,col}$, $P_{p,col}$ ($\mu mol\,m^{-2}\,d^{-1}$), and the $P_{p,col} : P_{cdom,col}$ ratio based on ocean color data from remote sensing. Also included are the $a_p : a_{cdom}$ ratio at 412 nm and open water area ($\times 10^3\,km^2$) (Xie et al., 2012). Keys for MRE, MS and CB are the same as those in Table 4.

		Apr	May	Jun	Jul	Aug	Sep	Annual
MRE	$a_p : a_{cdom}$	0.74	0.76	0.67	0.65	0.33	0.42	0.50
+	Area	2.2	12.3	43.1	63.5	74.5	74.4	74.5
MS	$P_{cdom,\,col}$	6.8	10.5	16.1	17.0	12.5	6.8	7.5
	$P_{p,col}$	2.7	4.2	5.9	4.1	2.1	1.0	1.8
	$P_{p,col} : P_{cdom,\,col}$	0.40	0.40	0.37	0.24	0.17	0.24	0.24
CB	$a_p : a_{cdom}$	0.76	0.49	0.42	0.31	0.28	0.27	0.30
	Area	0.25	12.5	43.9	58.9	74.0	79.0	79.0
	$P_{cdom,col}$	6.9	10.9	16.5	18.2	10.2	5.3	6.6
	$P_{p,col}$	3.3	2.9	3.6	2.7	1.5	0.7	1.1
	$P_{p,col} : P_{cdom,\,col}$	0.48	0.27	0.22	0.15	0.15	0.13	0.17

BGD
9, 16161–16211, 2012

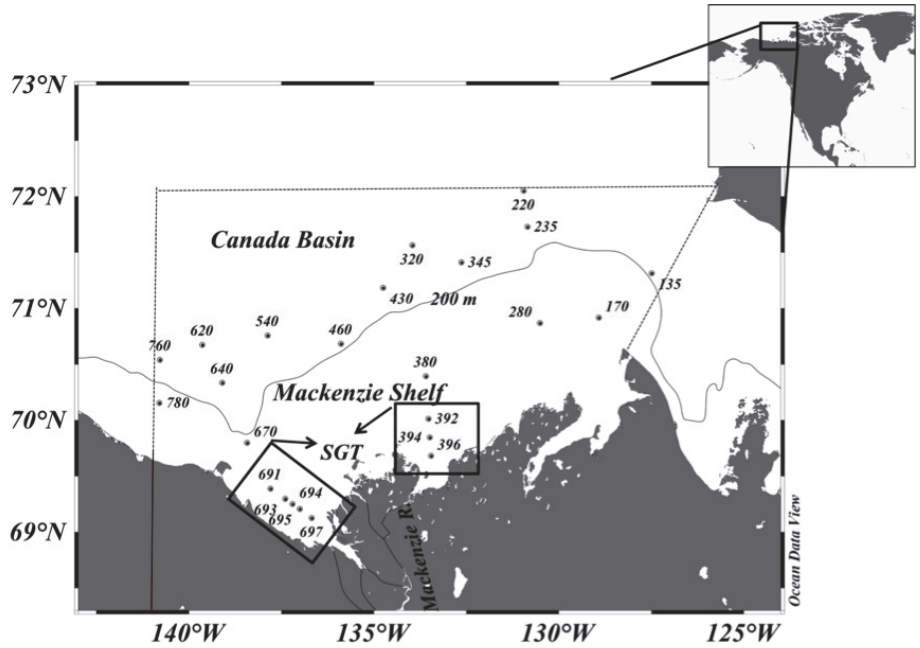

Fig. 1. Sampling map. See Table 1 for detailed sampling information for each station. Solid line is the 200-m isobath. Dashed line designates the area for which CO photoproduction rates were modeled. This map was constructed using the online software of Ocean Data View (Schlitzer, 2010, unpublished data, http://odv.awi.de).

BGD
9, 16161–16211, 2012

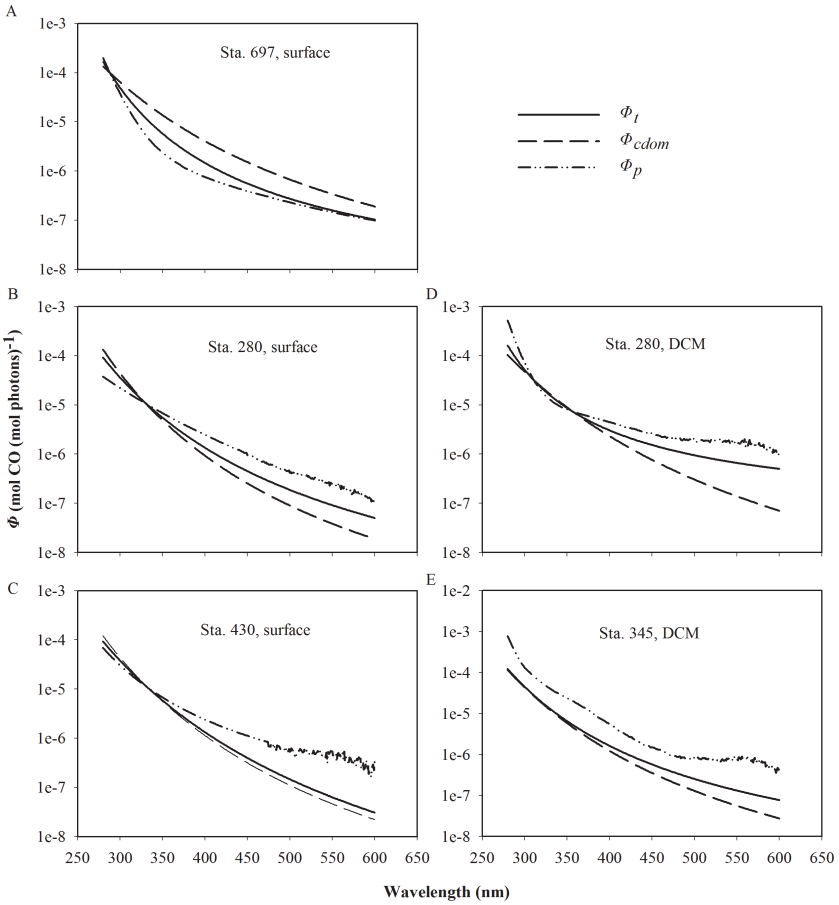

Fig. 2. Typical $\Phi_{cdom,\lambda}$, $\Phi_{p,\lambda}$, and $\Phi_{t,\lambda}$ spectra from the Mackenzie River estuary (Sta. 697), Mackenzie Shelf (Sta. 280), and Canada Basin (Sta. 345 and 430).

BGD
9, 16161–16211, 2012

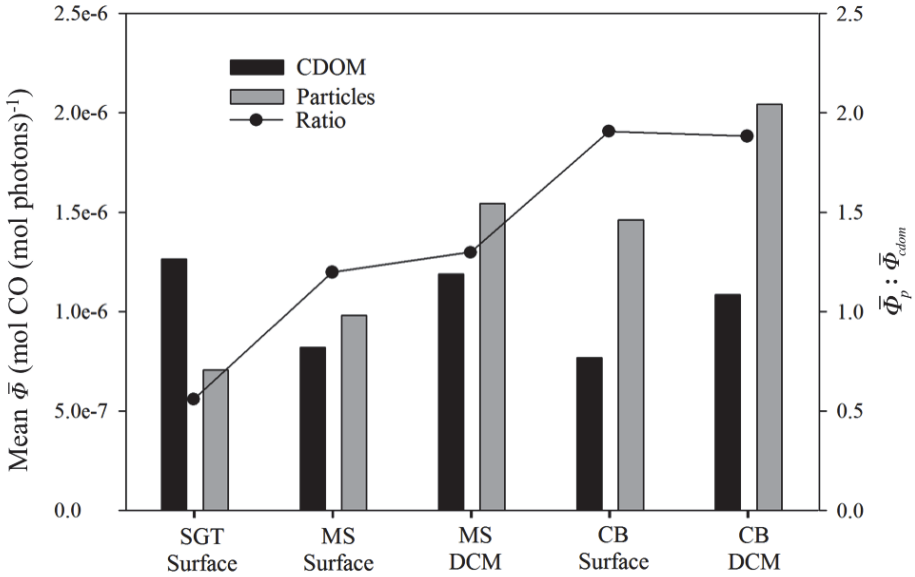

Fig. 3. Comparison of mean $\bar{\Phi}$ of particles and CDOM and the ratio of the two among the three sub-regions.

BGD
9, 16161–16211, 2012

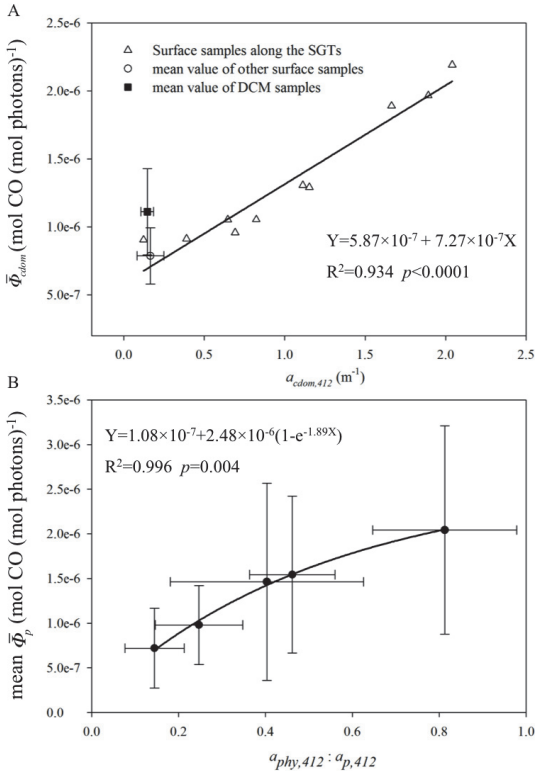

Fig. 4. Relationships between $\bar{\Phi}_{cdom}$ and $a_{cdom,412}$ **(A)** and between $\bar{\Phi}_p$ and the $a_{phy,412} : a_{p,412}$ ratio **(B)**. Error bars are one standard deviation. Solid lines are the best fits of the data (for the SGT samples only in **(A)**.

BGD
9, 16161–16211, 2012

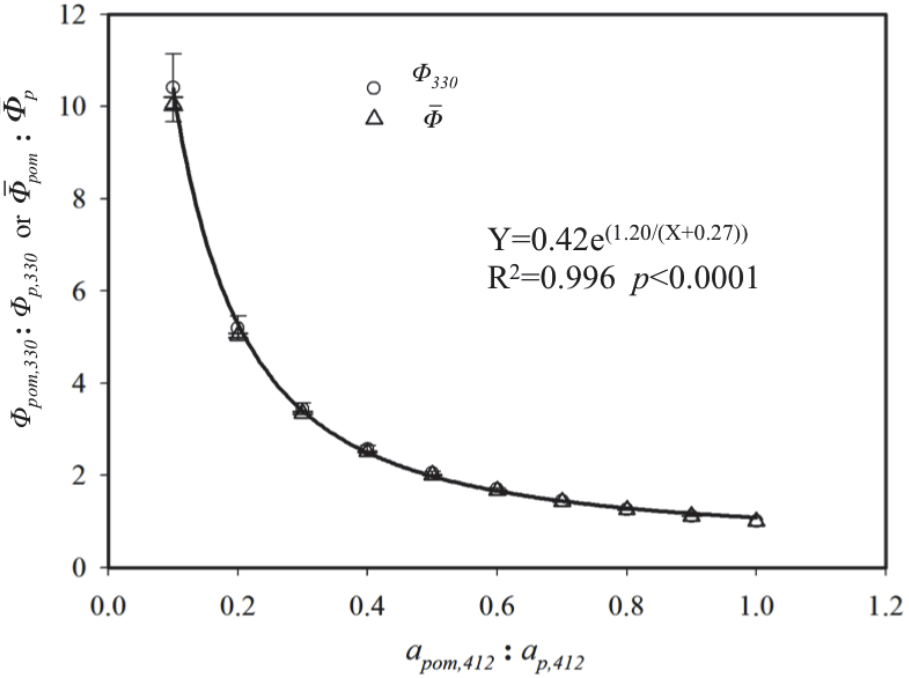

Fig. 5. Quasi-exponential relationship between the $\Phi_{pom,330} : \Phi_{p,330}$ (or $\bar{\Phi}_p : \bar{\Phi}_{pom}$) and $a_{pom,412} : a_{p,412}$ ratios along the SGTs. The two types of symbols are essentially overlapped at most $a_{pom,412}$: $a_{p,412}$ ratios. Solid line is the best fit of the mean of the $\Phi_{pom,330} : \Phi_{p,330}$ and $\bar{\Phi}_p : \bar{\Phi}_{pom}$ ratios to the $a_{pom\ 412} : a_{p,412}$ ratio. The $\Phi_{pom} : \Phi_p$ ratio shows negligible wavelength-dependence (data not shown). Error bars are one standard deviation among all stations in calculation.

BGD
9, 16161–16211, 2012

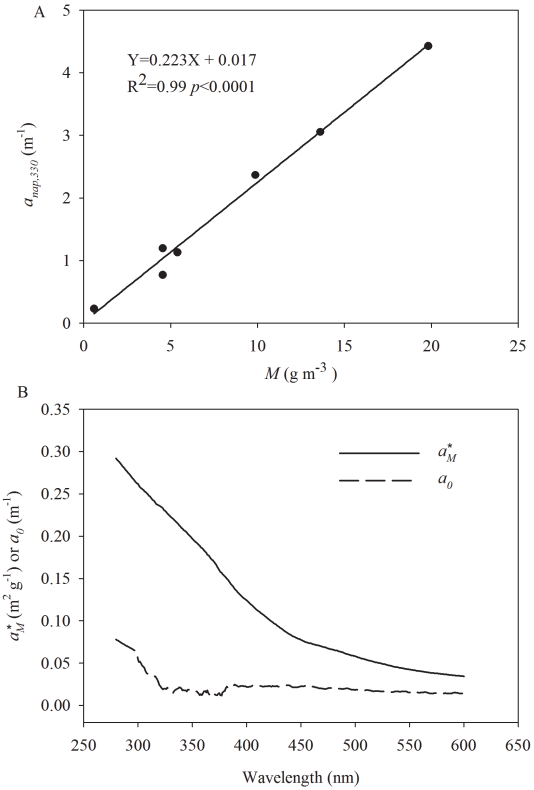

Fig. 6. Linear relationship between $a_{\mathrm{nap},330}$ and the concentration of suspended minerals **(A)** and spectra of the mass-specific absorption coefficient of minerals (a^*_M) and the absorption coefficient of remaining organics after pigment extraction (a_0) **(B)**.

BGD
9, 16161–16211, 2012

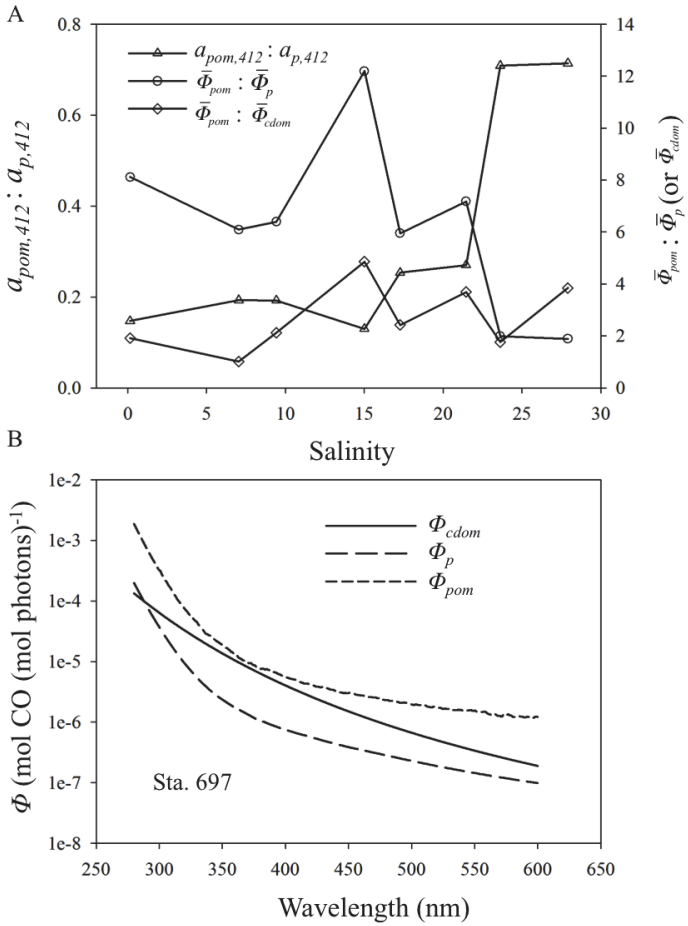

Fig. 7. Properties (ratios of $a_{pom,412} : a_{p,412}$, $\bar{\Phi}_{pom} : \bar{\Phi}_p$ and $\bar{\Phi}_{pom} : \bar{\Phi}_{cdom}$) vs. salinity plots for the salinity gradient transects in Mackenzie River estuary **(A)** and comparison of the Φ_{cdom}, Φ_p, and Φ_{pom} spectra from Sta. 697 **(B)**.

BGD
9, 16161–16211, 2012

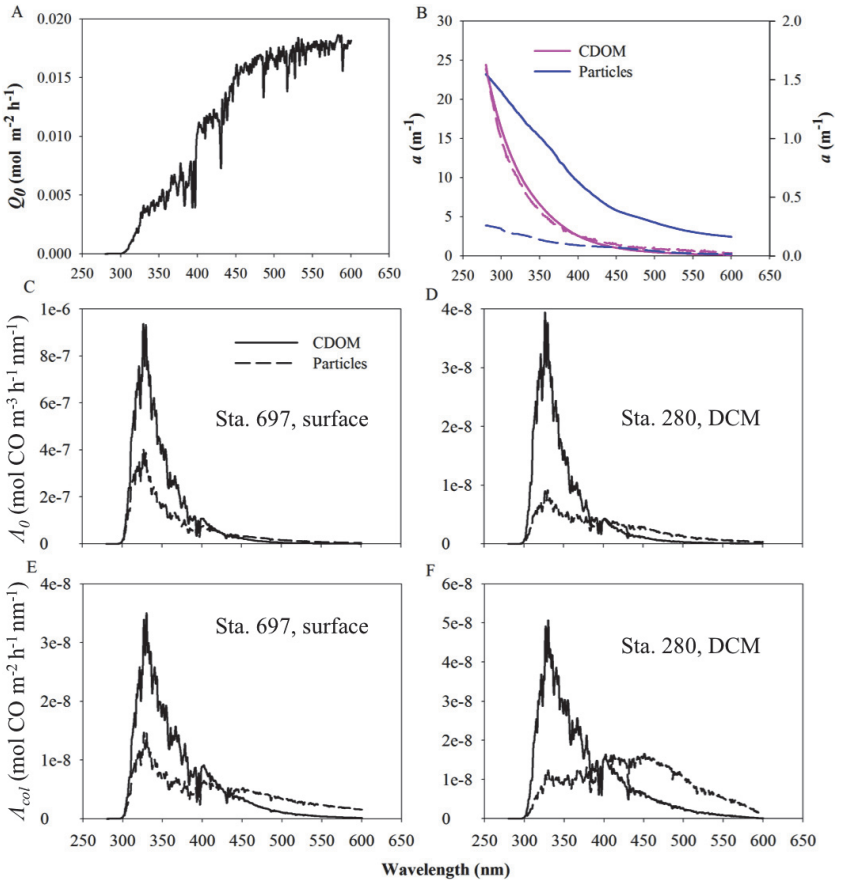

Fig. 8. Modeled surface spectral solar irradiance **(A)**, a_{cdom} and a_p **(B)**, surface CO action spectra (**C** and **D**) and depth-integrated CO action spectra (**E** and **F**). In **B**, left y-axis is for Sta. 697 (solid line) and right y-axis for Sta. 280-DCM (dashed line).

BGD
9, 16161–16211, 2012

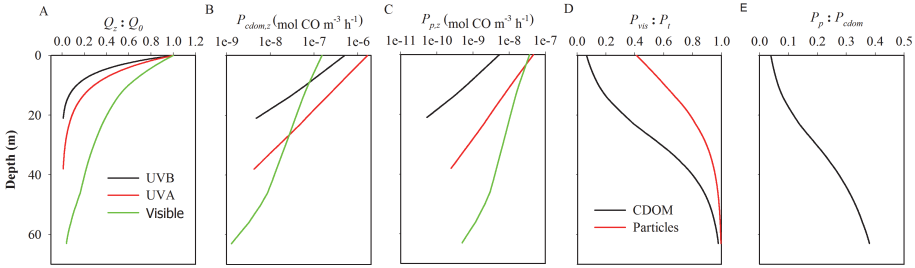

Fig. 9. Modeled vertical profiles of normalized solar irradiance **(A)**, CO photoproduction rate from CDOM **(B)** and particles **(C)**, the contribution of visible to full-spectrum CO photoproduction **(D)**, and the ratio of full-spectrum particle-based to CDOM-based CO photoproduction **(E)** at Sta. 430.

BGD
9, 16161–16211, 2012